GLYCOSYLATED CONJUGATED OLIGOMER AND CHLOROPHYLL BASED NANOPARTICLES FOR PHOTODYNAMIC THERAPY

A THESIS SUBMITTED TO

THE GRADUATE SCHOOL OF ENGINEERING AND SCIENCE

OF BILKENT UNIVERSITY

IN PARTIAL FULFILLMENT OF THE REQUIREMENTS FOR

THE DEGREE OF

MASTER OF SCIENCE

IN

MATERIALS SCIENCE AND NANOTECHNOLOGY

By

Ezgi Oduncu

January 2023

GLYCOSYLATED CONJUGATED OLIGOMER AND CHLOROPHYLL BASED NANOPARTICLES FOR PHOTODYNAMIC THERAPY

By Ezgi Oduncu

January 2023

We certify that we have read this thesis and that in our opinion it is fully adequate, in scope and in quality, as a thesis for the degree of Master of Science.

Dönüş Tuncel(Advisor)

Fatih İnci

Zeliha Soran Erdem

Approved for the Graduate School of Engineering and Science:

Orhan Arıkan
Director of the Graduate School

ABSTRACT

GLYCOSYLATED CONJUGATED OLIGOMER AND CHLOROPHYLL BASED NANOPARTICLES FOR PHOTODYNAMIC THERAPY

Ezgi Oduncu
M.S. in MATERIALS SCIENCE AND NANOTECHNOLOGY
Advisor: Dönüş Tuncel
January 2023

Nanomaterial-based therapeutic agents are drawing a lot of attention because numerous capabilities, including drugs, targeting groups, and photoactive units, can be combined on one platform to treat infectious diseases and cancer. In this regard, two different nanomaterials and their nanomedicine applications were reported. Firstly, red-emitting glycosylated conjugated oligomer (COL) nanoparticle was prepared and hybrid conjugation with gold nanoparticles was prepared by the nanoprecipitation method in order to examine photothermal applications. Due to their authentic electronic and optical characteristics, showing high singlet oxygen production ability, enabling control of the sizes of nanoparticles by acetyl groups in the side chains, enhancing their stability, and improving cell permeability via the hydrophobic effect they are promoting photosensitizers for photodynamic therapy. Secondly, chlorophyll, a natural photo absorbent, was extracted from spinach leaves, and chlorophyll nanoparticles were prepared by nanoprecipitation method because of their promoting properties which are high biocompatibility, low production cost, and natural reductive chemical atmosphere, containing plenty of hydrogen atoms and being environmentally friendly. Then, hybrid conjugation with gold nanoparticles was prepared to investigate photothermal therapy application. Both of the nanoparticles showed a high generation ability of reactive oxygen species (ROS) even at low light intensities and short exposure times which makes nanoparticles an ideal photosensitizer. From the antibacterial experiment, when Gram-negative (Escherichia coli, E. coli) bacteria were incubated with chlorophyll-based nanoparticles, a reduction up to 2.8-log and 2.33-log in colony-forming units (CFUs) was obtained under light irradiation for Chl-Au and Chl nanoparticles, respectively. Also, these nanoparticles showed minimal dark cytotoxicity (0.32-log and 0.15-log). On the other hand, conjugated

oligomer-based nanoparticles precipitated in bacterial suspension and were unable to pass across the cell wall of bacteria which was proved by SEM images and 4 mm and 5 mm inhibition zone were recorded for COL and COL-Au nanoparticles which are highly lower than ampicillin (7 mm). Along with these results, it is deduced that conjugated oligomer nanoparticles are not proper for antibacterial photodynamic applications although the interaction between the bacterial cell wall and nanoparticle was promoted with gold conjugation. For anticancer photodynamic therapy applications, MCF-7 breast cancer cells were treated with these nanoparticles in the dark and under white light illumination for 20 minutes, and the decline in cell viability was recorded at 50 %, 60 %, and 58 %, 72 % reduction for Chl, Chl-Au, and COL, Chl-Au nanoparticles, respectively. Also, they demonstrated dark cytotoxicity with the increment of concentration. Additionally, they also demonstrated the capacity for cellular imaging due to their inherent fluorescent properties, which might be used for image-guided PDT applications. Along with this, the cytotoxicity results were supported by displaying the cellular uptake of nanoparticles and their surrounding the nucleus of breast cancer cells.

Keywords: Photoactive conjugated oligomer, chlorophyll, photodynamic therapy, singlet oxygen, cancer treatment, antibacterial applications.

ÖZET

TÜRKÇE BAŞLIK

Ezgi Oduncu
Malzeme Bilimi ve Nanoteknoloji, Yüksek Lisans
Tez Danışmanı: Dönüş Tuncel
Ocak 2023

Nanomateryal bazlı birleşikler fotoaktif birimlere sahip olmaları, ilaç yükleme ve hedefleme grupları gibi bir çok işlevselliğe sahip olmaları ve bir çok özelliğin tek bir platformda birleştirebilmeye olanak sağladıkları için kanser ve bulaşıcı hastalıklara karşı tedavi aşamalarında büyük bir önem görüyor. Bu özellikleri dikkate alınarak iki farklı nanomalzeme ve bunların nanotıp uygulamaları rapor edilmiştir. İlk olarak, nanoçökeltme yöntemi ile glikosile konjuge oligomer bazlı nanomateryal (COL) ve bunun altın nanomalzeme ile hibrid konjugasyonu (COL-Au) hazırlandı. Eşsiz elektronik ve optik özellikleri, yan zincirlerdeki asetil grupları tarafından nanoparçacıkların boyutlarının kontrol edilmesini sağlamaları, kararlılıklarını artırmaları ve hidrofobik etki yoluyla hücre geçirgenliğini iyileştirmeleri nedeniyle, fotodinamik terapi için ışığa duyarlılaştırıcıları ajan olarak umut vaad ediyorlar. İkinci olarak, yüksek biyouyumluluk, düşük üretim maliyeti ve doğal indirgeyici kimyasal atmosfer, bol miktarda hidrojen atomu içeren ve çevre dostu olan teşvik edici özellikleri nedeniyle ıspanak yaprağından doğal bir fotosoğurucu olan klorofil elde edildi. Fototermal uygulamalarını incelemek için altın nanoparçacık ile hibrid konjugasyonu sentezlendi. Nanoparçacıkların her ikisi de, düşük ışık yoğunluklarında ve kısa maruz kalma sürelerinde bile yüksek bir reaktif oksijen türü (ROS) üretme yeteneği gösterdi ve bu da nanoparçacıkları ideal bir ışığa duyarlı ajan haline getiriyor.

Antibakteriyel deneyleri için, Gram-negatif (Escherichia coli, E. coli) bakteriler Chl-Au ve Chl nanopartiküller ile inkübe edildiğinde, ışık altında koloni oluşturan birimlerde (CFU'lar) 2,8-log ve 2,33-log'a kadar azalma kaydedildi.Ayrıca, bu nanoparçacıklar minimum karanlık sitotoksisite (0.32-log ve 0.15-log) gösterdi. Öte yandan, konjuge oligomer bazlı nanopartiküller, bakteriyel süspansiyonda çökelme gösterdiği ve bu bakteri hücresi duvarı ile istenilen şekilde etkileşime giremeyerek hücre duvarında toplandığı SEM görüntüleri gösterildi. COL için 4mm, COL-Au için 5 mm inhibisyon bölgesi kaydedildi. Bu sonuçlar etkinliği

kanıtlanmış olan ampisillinden (7 mm) oldukça düşüktür. Bu sonuçlarla birlikte, bakteri hücre duvarı ile nanopartikül arasındaki etkileşimin altın konjugasyonu ile desteklenmesine rağmen, konjuge oligomer nanopartiküllerin antibakteriyel fotodinamik uygulamalar için uygun olmadığı sonucuna varılmıştır.

Antikanser fotodinamik tedavi uygulamaları için MCF-7 meme kanseri hücreleri bu nanopartiküller ile karanlıkta ve beyaz ışık aydınlatması altında 20 dakika süreyle tedavi edilmiş ve klorofil bazlı hücre canlılığında COL ve COL-Au nanoparçacıkları için % 58 ve % 72, klorofil ve klorofil - Au nanoparçacıkları için % 50 ve % 60 oranında azalma kaydedilmiştir. Ek olarak, görüntü bazlı fotodaynamik uygulamaları için kullanılabilecek doğal flüoresan özelliklerinden dolayı hücresel görüntüleme kapasitesini de gösterdiler. Ayrıca, nanoparçacıkların kanser hücrelerinin çekirdeklerini sarmalaması ile hem sitotoksisite sonuçları desteklenmiş hem de hücre zarınından içeri girmesi kanıtlanmıştır.

Anahtar sözcükler: Fotoaktif konjuge oligomer, klorofil, fotodinamik terapi, singlet oksijen, kanser, antibakteriyel uygulamalar.

Acknowledgement

Firstly, I am thankful to my supervisor Prof. Dr. Dönüş Tuncel for her supervision throughout my master's studies.

Secondly, I am thankful to the examining committee members, Asst. Prof Fatih İnci and Asst. Prof. Zeliha Soran Erdem for their time to review my thesis.

Also, I want to state my deepest appreciation to Dr. Ayça Arslan Ergül and her students for their help and support. Finally, I would like to thank my family, especially my mom, and my lifemate for their support and help through this journey.

Contents

List of Figures

List of Tables

List of Abbreviations

CFU	Colony forming units
Chl	Chlorophyll
COL	Conjugated oligomer
CLSM	Confocal laser scanning microscopy
CONs	Conjugated oligomer nanoparticles
CPNs	Conjugated polymer nanoparticles
CPD	Critical point drying
DAPI	4',6-diamidino-2-phenylindole
DCFH	2,7-dichlorofluorescein
DLS	Dynamic light scattering
DMEM	Dulbecco's modified eagle medium
DMSO	Dimethyl sulfoxide
E.coli	Eschericha coli
EtOH	Ethanol
FT-IR	Fourier transfer infrared spectroscopy
LB	Luria-Bertani medium
LUMO	Lowest unoccupied molecular orbital
MIC	Minimum inhibitory concentration
MTT	Methyl thiazolyl tetrazolium
NIR	Near infrared
NMR	Nuclear magnetic resonance

NPs	Nanoparticles
OD_{600}	Optical density at 600 nm
PBS	Phosphate-buffered saline
PDT	Photodynamic therapy
PL	Photoluminescence
PS	Photosensitizer
ROS	Reactive oxygen species
S. aureus	Staphylococcus aureus
SEM	Scanning electron microscopy
THF	Tetrahydrofuran
UV-vis	Ultraviolet-visible

Chapter 1

Introduction

1.1 Conjugated Polymers and Oligomers

Conjugated polymers are organic and synthetic materials that have properties of electro- and photoluminescent. Due to the high reproducibility of the synthesis, the ease of establishing uniformity, and the ability to have greater control over end groups and molecular weight, oligomers, having convergent molecular properties with those of polymers, have attracted significant interest. [1] In addition to all these, the electrical conductivity of π-conjugated oligomers and polymers is increased by electrochemical doping, as they have a backbone with delocalized electrons. Due to those delocalized electrons, conjugated polymers and oligomers are conductive or semi-conductive in contrast to traditional insulator polymers and oligomers. Because of these appealing features, research efforts were focused on conjugated compounds and utilizing them in a variety of applications, including electronics, biomedicine [2, 3], solar cells, chemical sensing [4], biosensing [5], nanophotonics, etc. The structures of some commonly used conjugated polymers are given in Figure 1.1.

Depending on the intended use, oligomers may be preferable to polymers. For instance, in the construction of solar devices, oligomers may be favored over

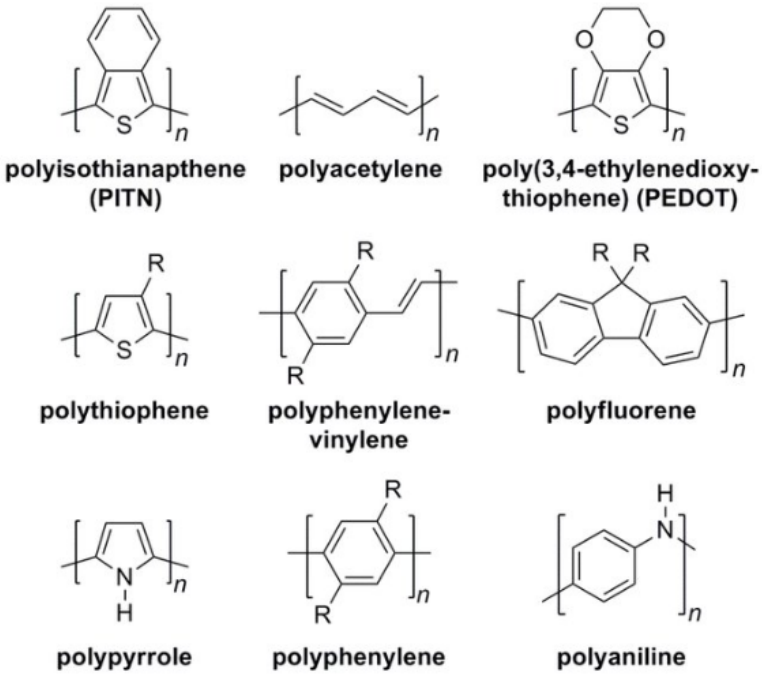

Figure 1.1: Common conjugated polymers. [6]

similar polymers that are insoluble or difficult to work with. [7] For imaging, monodisperse amphiphilic-conjugated oligomers have been developed. In order to create water-soluble, incredibly stable self-assembled particles in water, amphiphilic oligomers with fluorescence hues covering the full visible spectrum have been created. Co-assembling multi-targeting agents for bio-imaging is possible by the usage of oligomeric moieties which can self-assemble. [8]

1.1.0.1 Conjugated Polymer and Oligomer Nanoparticles

There has been attention to conjugated polymer-based nanoparticles (CPNs) because possessing combined characteristics of nanoparticles and conjugated polymers/oligomers for example having high fluorescence quantum yield and molar absorptivity, enabling functionalization with easy synthesizing, adjustable properties, requiring minimum cost and light-harvesting abilities. Self-assembled conjugated oligomer-based nanoparticles (CONs) are encouraging because they offer several advantages compared to CPNs that make them preferable for biological

applications. They have a fairly smaller size enabling improved cell penetration, cell permeability, and capability of excretion, and defining their molecular weight is easier. Also, CONs have better fluorescent quantum yields than CPNs and that can be comparable to CPNs in terms of stability and molar absorption. [9, 10] The preparation methods of CONs are decisive for determining the shape and size of nanoparticles. Examples of these methods are miniemulsion, redeposition, direct condensation of organic vapor, and pulsed laser ablation. [11]

1.1.1 Photophysical and Photochemical Properties of Conjugated Compounds

The electric conduction of the molecule can be determined according to their molecular orbital diagrams which indicate the relaxation type that can go through when excitation of its electrons by light. Photoluminescence (PL) is the generic name for fluorescence and phosphorescence and defines the emission of light from materials after they absorb photons. Most conjugated polymers show interesting photophysical properties, including PL, photoconductivity, etc., thanks to delocalized $\pi-$electrons, and are colored. The $\pi-$electrons of the conjugated oligomers are excited under light radiation with sufficient energy, going from the highest occupied molecular orbital (HOMO or ground state) to the next available energy state, the lowest unoccupied molecular orbital (LUMO). The excited electrons revert to the stable HOMO state by fluorescence or phosphorescence because the LUMO state is extremely unstable. The terms $\pi-$level (So) and *-level (S1) are also used to describe these orbitals. These materials have a typical band gap between the range of 1.5 eV to 4 eV, and their conductivity of electrical conductivity rises with a narrowing band gap. [12] At these levels of molecular energy, electron excitations can also happen in response to photon absorption, and the relaxation of these excitations back to the ground state can be taken place by different paths. The process of photon emission, which happens when electrons first cross into a triplet state and then come back to a singlet ground state that has lower energy than the lowest singlet excited state, is known as phosphorescence. Conjugated polymers display fluorescence. The Jablonski energy diagram

is displayed in Figure 1.2 and schematically represents these phenomena.

The differentiation between the HOMO and LUMO states in terms of energy, which defines the optical and electrical characteristics of the conjugated polymers, is called the band gap. The conjugated polymers' optical and electronic properties are tunable because the conjugated polymers' band gap is tunable. In this way, conjugated polymers become very attractive in many application areas. [13]

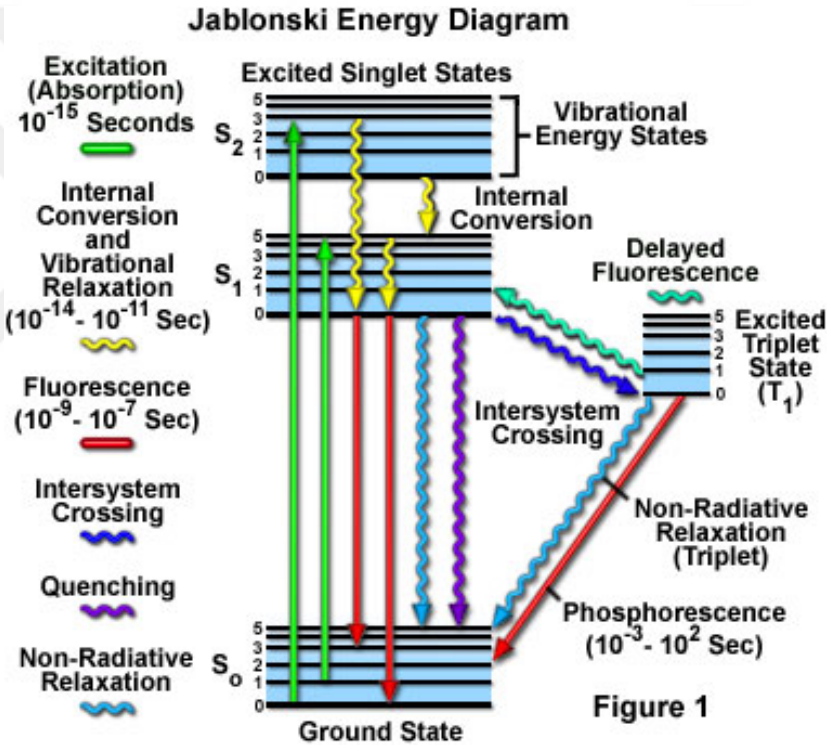

Figure 1.2: A simple illustration of Jablonski Diagram for photoluminescent phenomena. [13]

1.2 Nanoparticles Prepared from Pigments

For the production of nanoparticles, new and sustainable approaches under "Green nanotechnology" have recently been developing. In the sense of biocompatibility, low cost of production, and natural chemically reductive environment, using microorganisms (fungi and bacteria), along with natural products

(polysaccharides, and plant extracts), involving plenty of hydrogen atoms, for nanoparticle synthesis is highly advantageous in comparison to conventional synthesis methods. The techniques of nanoparticle synthesis from plant extracts are cost-effective, environmentally friendly, and done without complicated procedures. [14]

1.2.1 Chlorophyll

Tetropyls are described in organic chemistry as compounds consisting of four pyrrole or pyrrole-like rings loosely connected by carbon bridges of single-atom at the α positions of every ring. If tetropyls are formed by a closed structure, then tetrapyrrole is called macrocyclic, or generally simply cyclic. Metal cations can be attracted to macrocyclic tetrapyrroles and trapped at the core of the pyrrole frame, where a coordination complex is created. [15, 16] Porphyrins, chlorins, bacteriochlorins, and corrins are the main types of cyclic tetrapyrrole. While these groups generally share similar structural characteristics, only minor differences in hydrogenation degree result in a significant variety of their metabolic characteristics. The least hydrogenated groups are represented as porphyrins and the important prosthetic heme group is formed by a number of iron (Fe)-coordinated porphyrins. [17, 18] Chlorins are a more hydrogenated version of the tetrapyrrole archetype with a pyrrole transformed to pyrroline. The core structure of most chlorophyll is formed by chlorins. A fifth isocyclic ring connected to the macrocycle, substitutions one or more sides, a long chain of hydrocarbon (phytol) is included, and a magnesium (Mg) ion at the center are further characteristics of chlorophyll (Figure 1.3).

In fact, the majority of chlorophylls have a macrocycle of the chlorin type presenting a single bond at C7-C8, or the type of bacteriochlorin having a single bond in each sort of location. Due to the reduction of potential double aromatic bonds at C7-C8 and C17-C18 is preserved. The residue of phytol in the majority of synthetic and natural chlorophyll derivatives is eliminated through hydrolysis. In enzymatic reactions, the phytol can be a handle, it aggregates in micelles, and

the interaction between other pigments and cofactors and phytol is taken happen. All of these make phytol useful. The isolated macrocycle's photochemical characteristics are unaffected by removing it, despite the fact that its high lipophilicity is frequently unwanted in pharmaceuticals.

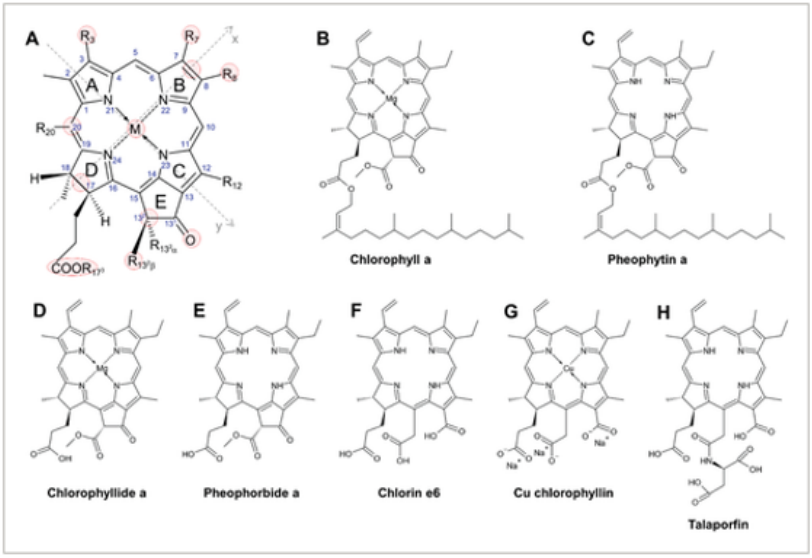

Figure 1.3: Structures of derivatives of chlorophyll. A) Chemical structure of a generical chlorophyll. Red highlights are placed on the chemical alteration locations that occur most frequently. B) Chlorophyll a and some relevant compounds (C,E) organically derived derivatives, D) a pioneer, and F–H) synthetic derivatives). [19]

The chemistry of both chlorophyll and its derivatives is determined by the tetrapyrrole moiety's aromaticity and the functional groups' reactivity found in side chains (Figure 1.3). The macrocycle has meso positions which are sensitive to electrophilic reactions. [20]

1.2.1.1 Photophysical and Photochemical Properties of Chlorophyll

Tetrapyrroles absorb light through $\pi - \pi^*$ transitions from their ground state (S0) to excited states (Sn) which is short-lived. Tetrapyrrole macrocycles exhibit two distinct bands in their visible and near-infrared absorption spectrum: B-band, also known as the Soret band, which occurs about 400 nm, and the Q-band, which

spans the wavelength range of 600–800 nm. The highest optical limit window for phototherapy (650-1350 nm), where the maximum amount of light can penetrate tissues, is where the Q-band is located. Comparing reduced tetrapyrrole macrocycles to porphyrins, chlorin and bacteriochlorin exhibit a gradually red-shifted Q-band. The structure of chlorophyll contains the isocyclic ring which causes redshifts in the visible tetrapyrrole absorption and increment in the intensity of it by decreasing the conjugated macrocycle symmetry. The Q-band is affected in different ways depending on the position of carbonyl groups of substituents: blue shift throughout the x-axis (C7), and redshift along the y-axis (C3, C131). On the other hand, substituents with carbonyl groups cause a red shift in the Soret band. The macrocycle's symmetry is increased by the chelation of a core metal, which causes the Q-band to shift to the blue, lose intensity, and split into two peaks. Internal conversion causes the rapid non-radiatively decay to the initial excited state, S1, from Sn excited levels. After excitation, the derivative of chlorophyll can come back to the ground state through three different processes. These processes are non-radiative vibrational relaxation, fluorescence, or moving by way of a triplet state (T1). The transition to a triplet state (T1) is caused by the intersystem crossing transition of a forbidden electron. Due to the extended lifespan of triplet states, relaxation from T1 to S0 can either be radiative (phosphorescence) or result from interactions with nearby chemical species in one of two ways: by transferring charges to molecular substrates for radical species formation, reactive oxygen species (ROS) is formed by a reaction between them, and oxygen (Type I reaction), or by energy transfer to the molecular oxygen($^3O_2$) ground triplet state directly, which leads the formation of singlet oxygen ($^1O_2$) (Type II reaction) (Figure:1.4). [21, 22]

Intermolecular interactions also affect the light activation of derivatives of chlorophyll. The aggregates formation is supported by disperse interaction and $\pi - \pi$, which alter the Q-band position by lowering its intensity. [24]

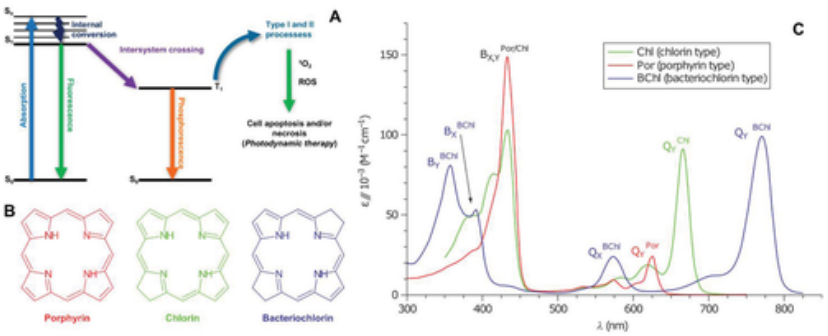

Figure 1.4: Photochemistry of chlorophylls. A) The excited chlorophyll derivatives' possible relaxation pathways are displayed in the Jablonski diagram. B) The types of chlorophylls photoactive compounds found naturally, C) The porphyrin-, chlorin-, and bacteriochlorin-type chlorophylls' spectra. [23]

1.3 Biomedical Applications of Conjugated Materials and Chlorophyll

The compatibility between cells and tissues and conjugated polymers were reported in vitro and in vivo, and have attracted interest in the biomedical field. [25] Since the 1980s, applications for in vivo imaging and monitoring [26], cell labeling, biomolecular sensing, and drug delivery have been explored. [27, 28] The main uses of CPNs in the biomedical field are shown in Figure 1.5.

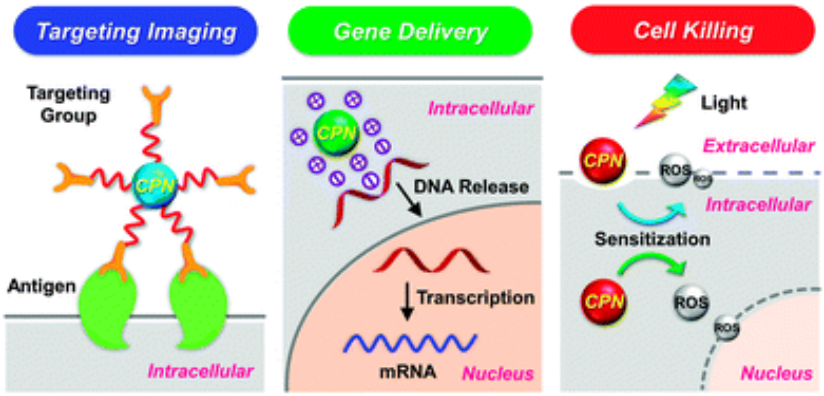

Figure 1.5: Schematic illustration of CPNs in different biological applications. [26]

High photostability, low cytotoxicity, and effective permeability through cellular cytoplasm are all achieved by conjugated-based nanoparticles. Organic dyes

and fluorescent proteins are frequently used in imaging in biology, however, they exhibit rapid photobleaching, which is a significant disadvantage. In addition to these regularly used biological materials, quantum dots are a synthetic substitute for CPNs, but they require great care because their heavy-metal cores are very cytotoxic. Conjugated polymers are more suited for live cell imaging because they offer better light-harvesting and signal-amplification capabilities, higher fluorescence brightness and photostability, and naturally reduced cytotoxicity. [29]

Similarly, chlorophyll and its derivatives possess special qualities and high potential in the domains of science and medicine. Indeed, they can be utilized as cancer-preventing agents, antimutagen, agents to induce apoptosis, efficient antioxidants, and antibacterial and immuno enhancing compounds. [23]

1.3.1 Drug Delivery and Imaging

The term "drug delivery" refers to the process of sending certain drugs to their intended recipients over a period of time by using pharmaceutical formulation techniques, encapsulation techniques, improving the drug loading efficiency of particular carriers, and other approaches. [30, 31] Despite the fact that various effective anticancer medications have been developed for more than a century, effective cancer therapy still poses a difficulty. It is obvious that there are not any effective drugs by their nature. The effectiveness of drugs is explained by how well they are managed and transported. Drug delivery methods that are effective are still insufficient. The low water solubility of hydrophobic anticancer drugs limits their usage in biological mediums. Additionally, there might be side effects and this could harm healthy cells. [32]

Organic dyes and fluorescent proteins are frequently used in bioimaging, however, they exhibit rapid photobleaching, which is a significant disadvantage. For imaging of cells, conjugated polymers are convenient since their promising properties are better harvesting of light capacity, signal amplification capability, photostability, high brightness of fluorescence, and having less cytotoxicity by their nature. [33]

In the literature, some charged conjugated polymers are accounted for intracellular imaging biomolecular application that does not promote any particle formation or require bioconjugation. [34]

The nanomaterials containing anionic groups like phospholipids promote electrostatic attractions which help the binding of cationic polymers to the surfaces of cells easily. However, there might be nonspecific electrostatic interactions that make it difficult to control cellular uptake. On the other hand, it has been claimed that cell permeability and charges of apoptotic cells are higher than healthy cells. In this regard, apoptosis of cells can be monitored by cationic ones. The reason for this is the addition of negative charges besides their negative charge by nature. [35]

1.3.2 Cancer Therapy

The International Agency for Research on Cancer estimates that 29.5 million people will die from new cancer cases and 20.4 million from cancer-related mortality each year by 2040. In the United States, 1.81 million new incidences of cancer were stated in 2020, and approximately 607,000 people died of cancer, according to the National Cancer Institute (NCI). In this regard, a major worldwide health issue is cancer. The primary cause of cancer mortality and morbidity is metastasis [36]. The spread of cancer cells to adjacent tissues and organs from the site where they first developed is known as metastasis. They leak into the blood and lymphatic systems as they leave the main tumor. Apoptosis, autophagic death, pyroptosis, and necrosis are the four different forms that occur in the death of cells (Figure: 1.6). Apoptotic cells undergo swelling and packing densely with intercellular organelles. Generally, expanding the mitochondria and other organelles of necrotic cells, rupturing the membranes, and leaking the organelles are typical characteristics of necrotic cells. Double membranes and autophagosomal vacuoles with cytoplasmic contents are features of autophagic cells. [37]

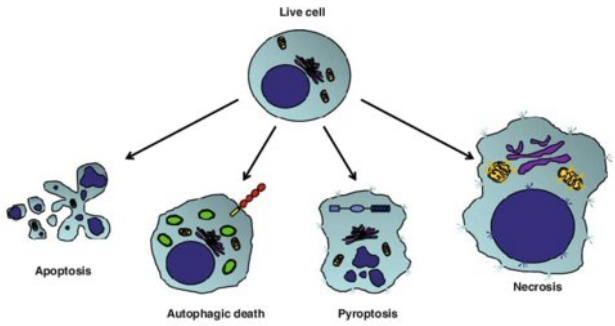

Figure 1.6: Scheme for different forms of cell death. [38]

1.3.2.1 Chemotherapy

Traditional chemotherapeutic medicines and cytotoxic medications are the main treatments utilized to treat cancer from a fundamental perspective. To kill and inhibit the growth of tumors, chemotherapeutic drugs are being used. [39] On the other hand, there are several drawbacks of traditional chemotherapy that restrict its efficiency of the chemotherapy. The solubility and stability of agents used in chemotherapy are weak, resistance to drugs, targeting that is not selective, and releasing chemotherapeutic agents without control are some of them. In spite of the negative aspects, chemotherapy is the most used and effective method of cancer treatment. However, the efficiency can increase by combination with other therapies, and improve the efficiency of chemotherapy. Thanks to the supramolecular approach, while limited drawbacks the efficiency of chemotherapy can increase because they are promoting vehicles for drug delivery with the encapsulation of drugs.

1.3.2.2 Phototherapy

Phototherapy known as light therapy is one of the medical treatments that use both artificial light sources and daylight used to treat cancers and skin disorders like infection and mood and sleep disorders. There are two types of phototherapy; photothermal therapy (PTT) and photodynamic therapy (PDT) (Figure: 1.7). For phototherapy, the photoreactive agent that is activated with light is used to

inactivate pathogens. The excitation of the PTT or PDT agent has resulted in thermal and chemical damage in the tumor respectively. [40, 41]

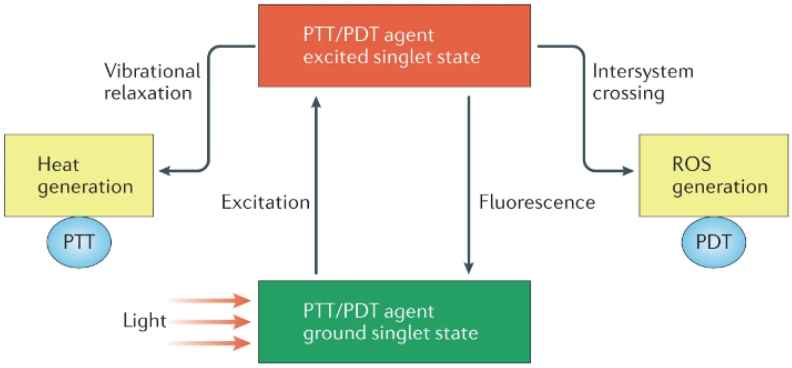

Figure 1.7: Clinical advancement and possible of photothermal and photodynamic for cancer treatment. [42]

Chemotherapy and radiotherapy treatments are often used in cancer treatment. However, as a result of these treatments, serious side effects such as anemia, gender and fertility problems, and hair loss can be seen in patients. Photodynamic therapy serves as an alternative method due to its advantages such as less cost and insignificant side effects. [43, 44]

1.3.2.3 Photothermal Therapy

In PTT, the photothermal agent absorbs energy from photons when light is applied at a specific wavelength, and the transformation occurs from a ground state to an excited singlet state. [40]

Following, the vibrational relaxation on the excited singlet state, the excited photothermal agents collide with their surrounding molecules. This collision causes excited photons to return to the ground state, and increase kinetic energy. This raise in energy, increase the temperature of this environment which causes the inactivation of pathogens like tumor ablation and necrosis (Figure: 1.8). [42]

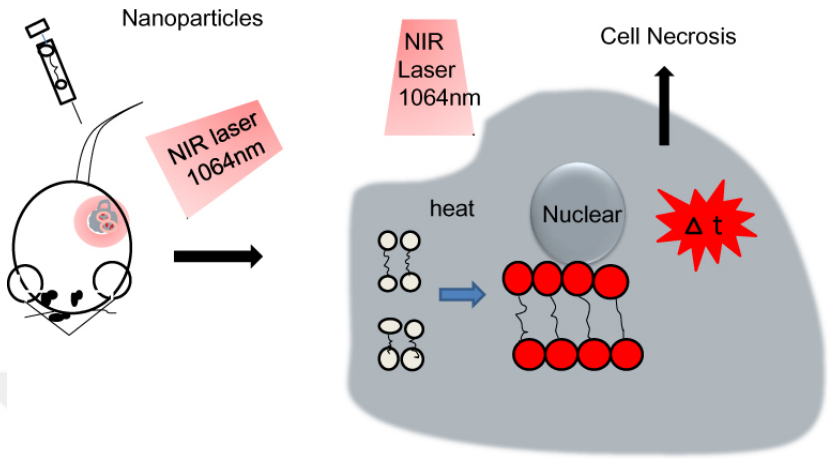

Figure 1.8: Pathological Mechanism of Nanoparticle-Based Photodynamic Therapy and Photothermal Therapy. [45]

1.3.2.4 Photodynamic Therapy

The main principle of PDT is photochemical reaction chains induced by a photoactivated PS drug. These reactions trigger reactive oxygen species (ROS) generation to cause cytotoxic effects. In photodynamic therapy, there are three main components; a photosensitizer, molecular oxygen, and light. The excitation of PS with proper light exposure leads to the formation of reactive oxygen species (ROS) ranging from peroxides, hydroxyl radical, and singlet oxygens from the molecular oxygens in order to promote the death of cells and tissues as shown in Figure 1.9. [46] When an appropriate wavelength is applied, the PS drug is activated with the absorption of photons to the excited singlet(S1) state, and with the intersystem crossing, it is transitioned to the excited triplet state (T1) and relaxation. The T1 state lifetime is longer than the S1 state. This situation extends the interactions between PS in the T1 states and its surrounding molecules. The reactive oxygen species (ROS)production is triggered by the excited triplet state through two mechanisms as displayed in Figure 1.10; reactive oxygen species (ROS) can be created by T1 PS directly oxidizing biomolecules (Type I mechanism) or by reacting with O_2 to create singlet oxygen ($^1O_2$) (Type II mechanism).

In type I reaction, an electron is transferred from the excited photosensitizer

to the substrate in order to create free radicals. The photosensitizer receives an electron from the substrate, which makes it a radical anion and causes the generation of substrate cation. When there is oxygen in the environment, the oxygenated product of superoxide anion or hydroxyl radical is produced depending on the situation by reaction with oxygen. These substances are useful in the battle against pathogenic microbes because they modify the functionality of cells or tissues in creatures that are exposed to them.

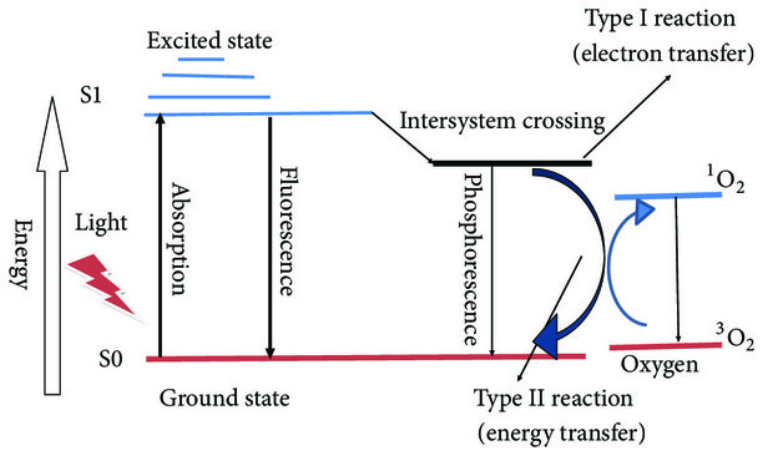

Figure 1.9: Type I and type II reactions. [46]

In type II reaction, the excess energy of excited sensitizer is transferred between the triplet state and molecular oxygen in a ground state leading to the excitation of singlet oxygen.

Because the Type II mechanism causes the majority of the cell damage brought on by PDT, oxygen is required for PDT to be effective. It is crucial that PS is concentrated in tumors at the time of irradiation because of the brief half-lives of ROS (for example, the effective radius of $^1O_2$ is only 20 nm). [40]

PDT is used in clinical settings, as seen in Figure 1.11. Following administration, accumulation of PS throughout the body is seen. After that, PS is accumulated in the targeted tissue and when light is illuminated, the target tumor will be killed. Cell destruction in PDT primarily depends on apoptosis.

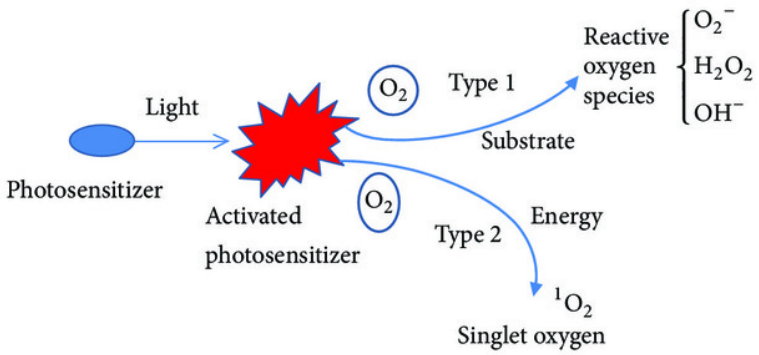

Figure 1.10: The illustration of the production of singlet oxygen and reactive oxygen species. [46]

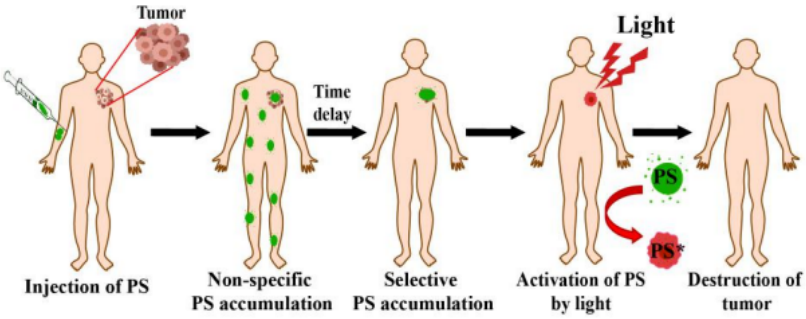

Figure 1.11: PDT in clinical practice. [47]

In comparison to other conventional medicines, PDT has less invasiveness, better targeting capabilities, and fewer side effects with a clinically authorized antibacterial and anticancer approach. PDT, however, has a number of drawbacks, such as limited light penetration depth that makes it difficult to treat superficial cancers, oxygen dependence that prevents it from treating hypoxic tumors, and self-catalyzation of traditional PSs. The combination of many treatment strategies helps to overcome these limitations and improve the effectiveness of therapy.

Özkan et al. investigated antibacterial and anticancer phototherapy applications of red-emitting conjugated oligomer (COL) based nanoparticles (COL-Au-NPs) on bacteria and breast cancer cell lines. The amine pendant groups lead to toxicity in dark, and the remarkable reduction was achieved by capping with

cucurbit[7]uril (CB7@COL-Au-NPs). (Figure 1.12) [48]

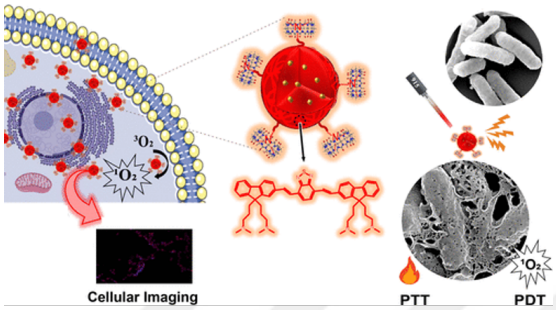

Figure 1.12: Schematic display of the nanoparticles and their antibacterial and anticancer phototherapy applications (Reprinted with permission from [48]. Copyright 2020, American Chemical Society).

Zhao et al. studied the antibacterial photodynamic efficiency of a cationic conjugated oligomer (OPV) with porphyrin photosensitizer against E. coli and S. aureus. They displayed high ROS generation capability even at low concentrations (33 and 88 nM). Also, the presence of cationic donors enhanced the solubility of water and reduced porphyrin aggregation. (Figure 1.13) [49]

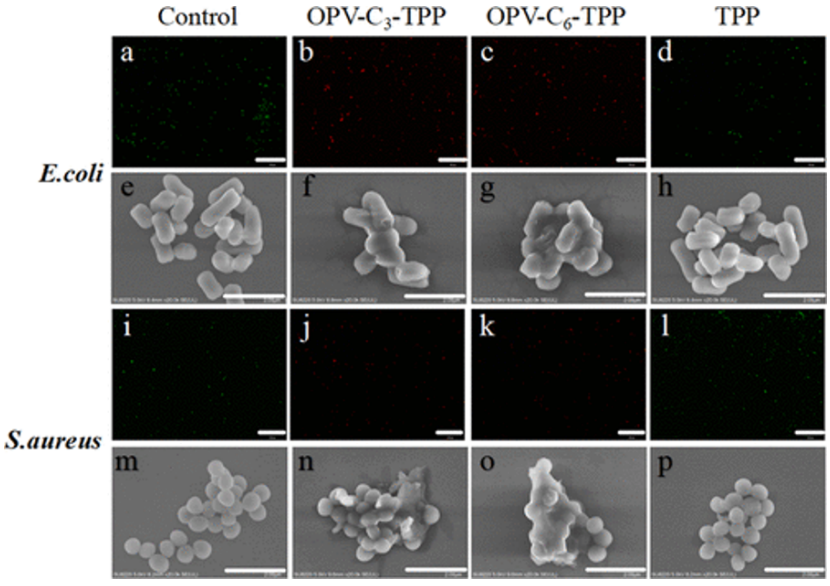

Figure 1.13: The SEM images of E. coli treated with OPV-C3-TPP and control groups under white light illumination for 1 h. [49]

On the other hand, chlorophylls cannot be used directly in drugs that must pass through the cell membrane unaltered due to their chemical structure. As a

result, its concentration in tumor cells is reduced due to its sensitizing activity and ability to dissolve in aqueous solutions. In other words, in aqueous and biological mediums, purified chlorophylls show poor solubility in organic solvents and are insoluble in water. They agglomerate into less photoactive materials that make them inappropriate for use in the formulation of intravascular drugs due to the lipophilicity of the porphyrin aromatic ring. [50] The effect of the phototherapeutic of PSs is enhanced by the combination of nanomaterials in terms of raising the solubility and stability, and efficiently conveying them into malignant tumors. The simplicity of surface conjugation between PSs and metallic nanoparticles makes metallic nanoparticles excellent nanocarriers. [51]

Shaimaa Alexeree et al. reported the conjugation of chlorophyll b and gold for improving their photodynamic efficiency toward MCF7 and the HepG2 cancer cell lines. Chlorophyll b and gold nanoparticles were synthesized from natural sources, spinach, and potatoes, respectively. The results indicated that this nanoconjugate with a higher concentration of 10.6 mg/mL has low dark toxicity and excellent killing efficiency against tumor cells under 650 nm laser irradiation. (Figure 1.14) [52]

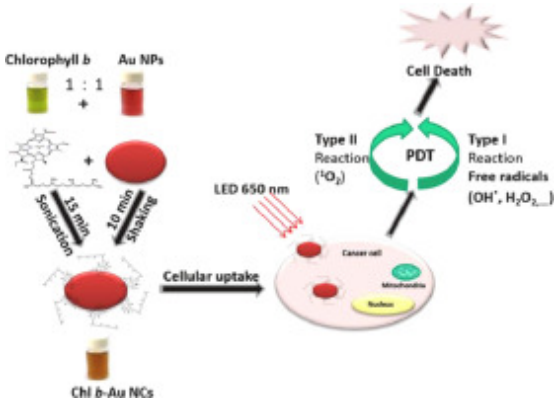

Figure 1.14: Schematic illustration of preparation Chl b-Au nanoconjugate and its PDT application. (Reprinted with permission from [52]. Copyright 2021 Elsevier B.V.)

Yu-Cheng Chin et al. reported a clustered nanoparticle by assembling Iron oxide and chlorophyll as photosensitizers. The cluster-structured nanoparticles

(CNPs) were prepared by a facile one-pot coprecipitation method. The internalized Fe-based nano-photosensitizers were utilized both in vivo and vitro. The survivability rate of orthotopic MB49-bearing mice was significantly increased to 91.7% as well as preventing tumor growth.(Figure 1.15) [53]

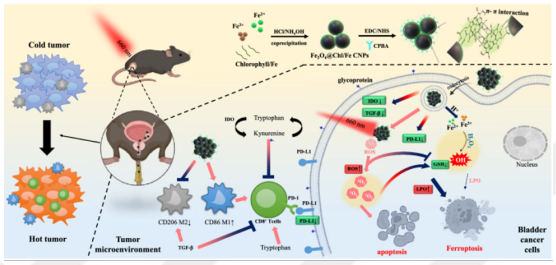

Figure 1.15: The illustration of the synthesis of iron oxide@chlorophyll clustered nanoparticles for targeted delivery and immunoregulatory effect within BC cells. [53]

Rongjun Liu et al. synthesized a novel spinach-based and carbon-based nanomaterial namely "chlorophyll-rich biomass quantum dots" (CBQDs) and its conjugation with copper ions in order to increase the efficiency of PDT by decreasing biothiol concentrations in tumor cells. These nanoparticles showed high ROS generation efficiency against tumor cells without any detection of tumor cells after 12 days. Additionally, they exhibited low cytotoxicity and excellent biocompatibility with concentrations from 50 and 500 µg mL^{-1}. (Figure 1.16) [54]

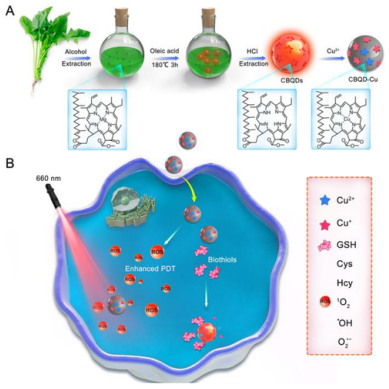

Figure 1.16: A) CBQDs and CBQD-Cu nanocomposites preparation shown schematically and B) the imaging implementation of intracellular biothiol and dual-enhanced PDT against cells. [54]

1.3.2.5 Development of Antimicrobial Agents

In recent years, antibiotics have been very effective in combating pathogens and have played a vital role in extending the human lifespan. However, when antibiotics are used excessively, microbial strains that are resistant to antibiotics emerge. As a result of this situation, antimicrobial treatment becomes more difficult. Alternative antimicrobial treatments are urgently sought to alleviate the crisis because it is important to avoid the risk of antibiotic resistance. [55, 56, 57, 58] Alternative approaches like surfaces with smart bacteria and anti-biofilm are being studied in order to fight infections caused by bacteria and the formation of biofilm. [59] Supramolecular materials have promoting properties which are having special properties such as advocating controllable and flexible interactions and making assembling different agents possible. These properties make the supramolecular approach advantageous. [60] PDT and PTT methods can also be effective to combat killing bacteria. Pathogens, such as viruses, have been treated with antimicrobial PDT. (Figure 1.17)

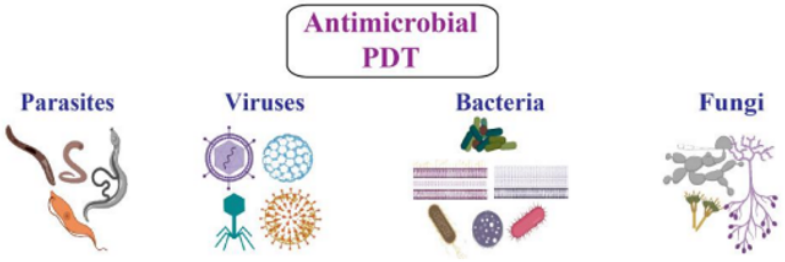

Figure 1.17: Pathogen types that can be killed by PDT. [47]

Peng et al. examined the photothermal and photodynamic efficiency of OFGreen-N, a fluorene-based conjugated oligomer, against E. coli. The oligomer (10 μg/mL) showed excellent photothermal efficiency under 808 nm laser illumination, and the conversion efficiency was reported as 37.7%. A significant reduction in the number of E. coli was reported by treating OF-Green-N (0.06 mg/mL) under light illumination. Moreover, since OF-Green-N has quaternary ammonium groups in its structure this nanoparticle displayed high dark cytotoxicity (Figure 1.18) [61]

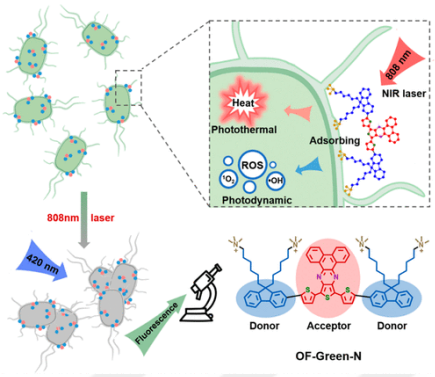

Figure 1.18: Schematic illustration of killing bacteria by OF-Green-N. (Reprinted with permit from [61]. Copyright 2020, American Chemical Society)

Vahhab Soltaninejad et al. synthesized bifunctional PVA/ZnO/AgI/Chlorophyll nanocomposite film and investigated its antimicrobial properties against E. coli and S. aureus. For the S. aureus and E. coli cell lines, the inhibition zone has been assessed at about 20 and 12 mm, respectively. Also, it has been reported that the high-yield result is obtained by LED lamp irradiation (70 W, λ = 425 nm) for 60 min. (Figure 1.19) [62]

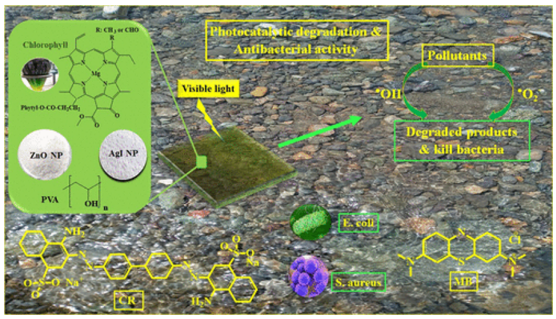

Figure 1.19: The schematic representation of bifunctional PVA/ZnO/AgI/Chlorophyll nanocomposite film and its promoting applications. [62]

1.4 Aim of the Study

The main goal of this study is to synthesize chlorophyll and prepare conjugated oligomer and chlorophyll nanoparticles and their hybrid conjugations with the

gold nanoparticle, and use them as photosensitizers in the antibacterial and anticancer PDT and imaging process. The nanoprecipitation method was used to prepare nanomaterials.

Chlorophyll was intentionally selected since cyclic tetrapyrroles are naturally proven photosensitizers because they absorb strongly in the visible region of the electromagnetic spectrum, have a high molar extinction coefficient when activated by visible light their capacity to produce singlet oxygen, and also have low dark toxicity. In this regard, chlorophyll, a natural photo-absorbent, was synthesized from spinach leaf, and chlorophyll nanoparticles and hybrid conjugation with gold nanoparticles were prepared. The novelty of synthesized chlorophyll is containing both chlorophyll a and chlorophyll b as well as the method used for preparing nanomaterials.

In detail, chlorophyll is made up of four pyrrole rings that are linked together structurally by a magnesium ion and a long hydrophobic alkyl chain. Additionally, one of the pyrrole rings in chlorophyll has a methyl group (-CH_3) linked to it in chlorophyll a and the formyl group (-CHO) takes the place of the methyl group (-CH_3) in chlorophyll b. The conjugation mechanism is taken place by a coordination bond formed between Lewis acid and Lewis base. In this situation, the Mg atom at the center of Chl molecules is Lewis acid, and the interaction between protein and other molecules and the Mg atom is formed through coordination bonds. In this regard, the gold nanoparticle is encapsulated by chlorophyll a which leads to an improved intersystem crossing and promotes the generation capability of ROS. Also, by taking advantage of the positive charges provided by the formyl group (-CHO), the electrostatic reaction between them and negative charges located on the surface of the gold nanoparticle was formed in order to both eliminate the minimal solubility of chlorophyll and increase the light-induced effect.

Additionally, the synthesized red-emitting conjugated oligomer was characterized, and the hybrid conjugate with gold nanoparticles was prepared. Red-emitting conjugated oligomer (COL) has acetyl groups in the side chains making it possible to control the nanoparticle's size, increase stability, and enhance cell

permeability via the hydrophobic effect. While the core of the oligomer is hydrophobic, side chains are hydrophilic. Therefore, by taking advantage of this, it is expected to achieve specific binding between mannose receptors and acetylated mannose groups in cell walls. Also, since Chl, Chl-Au, COL and COL-Au nanoparticles showed a high yield of reactive oxygen species (ROS) generation, their photodynamic therapy application against both gram-positive and gram-negative bacteria and cell lines was investigated. While they have low dark cytotoxicity against human breast cancer cells (MCF-7), displayed a high level of cytotoxicity with light illumination. Moreover, due to their inherent fluorescent nature, their cellular imaging capacity was displayed which makes them good candidates for drug-loaded and image-guided therapy applications.

Moreover, since all of the nanomaterials are hydrophobic, because of their hydrophilic characteristics, Au NPs can dramatically increase photosensitizers' solubility in water and boost cellular uptake.

Chapter 2

Experimental

2.1 Materials

Analytical-grade chemicals were utilized in the chemical synthesis and used after being taken. Whenever necessary, Milli-Q water (18.2 M cm at 25°C) was used. After distilling and drying the solvents required, experiments and reactions were conducted under air, unless otherwise specified. The deuterated solvents (DCl_3 and D_2O) required to run NMR spectroscopy were bought from Merck. The required solutions and chemicals for mammalian cell culture; Dulbecco's Eagle Medium (DMEM) and sodium pyruvate, fatal bovine serum (FBS) penicillin/streptomycin (Pen-strep), and MEM non-essential amino acids solution were bought from Sigma-Aldrich, Thermo Fischer Scientific, and Merck, respectively.

For passaging process, the required Gibco Trypsin-EDTA (0.25%) solution being bought from Sigma-Aldrich was used. PBS (10X), which was acquired from Sigma-Aldrich, was diluted 10-fold to make 1X PBS by distilled water and autoclaved and stored until usage. In order to measure the cell viability of nanoparticles, MTT was bought from Sigma-Aldrich was used. For preparing the fixation solution required for the imaging process, 37% paraformaldehyde solution was

bought from Carlo Erba Reagents, and Triton X-100 detergent was supplied from Merck. The dye for imaging by confocal laser scanning microscopy, DAPI was purchased from Thermo Fischer Scientific.

2.2 Instrumentation

2.2.1 ^{1}H Nuclear Magnetic Resonance (NMR) Spectroscopy

Utilizing a Bruker AVANCE DPX-400 NMR spectrometer running at 400 MHz for ^{1}H NMR chemical structures of substances were characterized.

At 25°C, all of the spectra were captured while products were being dissolved in deuterated solvents. Chemical shifts were expressed in ppm with respect to the internal standard, tetramethylsilane (TMS). The abbreviations for spin multiplicities are s (singlet), d (doublet), t (triplet), q (quartet), and m (multiplet).

2.2.2 Electrospray Ionization-Mass Spectrometry

In order to analyze the product's exact molecular weight, Agilent 6224 Accurate-Mass Time-of-Flight (TOF) LC/MS and Agilent 6530 Accurate Mass Q-TOF LC/MS systems were engaged.

2.2.3 F T -IR Spectroscopy

Fourier Transform Infrared spectra were measured using a Bruker Alpha-II Platinum ATR FT-IR spectrometer outfitted with a DLATGS detector with a resolution of up to 2 cm^{-1} in order to characterize the chemical functional groups on the chlorophyll. The data were captured in the 4000-400 cm^{-1} spectral band for

scans.

2.2.4 UV-Vis Absorbance Spectroscopy

Ultraviolet-visible (UV-Vis) optical characterization spectra were obtained by Cary 300 UV-Vis Double Beam Spectrometer equipped with a Xenon-lamp as the source of illumination. UV-Vis absorbance of compounds was recorded between the wavelengths of 200 nm and 800 nm, by using quartz cuvettes with 1 cm width. Water was used as a solvent.

2.2.5 Fluorescence Spectroscopy

The fluorescence spectrum of samples was obtained at the solution phase using a Varian Cary Eclipse fluorescence spectrophotometer. A quartz cuvette having a 10 mm path length was used.

2.2.6 Dynamic Light Scattering (DLS) and Zeta Potential

The size and zeta potential of particles were obtained by Malvern Zetasizer Nano ZS equipped with a 663 nm laser at 25°C. Two different cuvettes were used; while in order to measure the zeta potential folded capillary zeta cells were used, DLS results were examined with a standard fluorescence cuvette.

2.2.7 Scanning Electron Microscopy (SEM)

The morphological characterization of nanoparticles was examined with Quanta 200 FEG Thermo Fisher Scientific operating at environmental scanning electron microscopy mode.

2.2.8 Transmission Electron Microscopy (TEM)

The morphological properties of nanoparticles were visualized with FEI Tecnai G2 F30 transmission electron microscope.

2.2.9 Microplate Reader

The Optical density (OD) value of bacteria was measured at 600 nm (OD_{600}), and for the MTT assay, the absorbance values were recorded at 570 nm with SpectraMax M5 multi-detection microplate reader system.

2.2.10 Confocal Laser Scanning Microscopy (CLSM)

CLSM images were obtained on Leica TCS SP8 X multiphoton system with a 40X objective.

2.2.11 Critical Point Dryer (CPD)

The Autosamdri-934 Tousimis CPD in a cleanroom was used to dry samples by CO_2 at 7.4 MPa, 30°, and for intermediate fluid, ethanol is used.

2.3 Syntheses

2.3.1 Extraction of Chlorophyll

Firstly, spinach leaves were rinsed with distilled water 4 times. Then they were cut into small parts, and dried in an oven for 3 h, at 40 ^0C. Secondly, 100g was weighed and placed in 250-300 mL of ethanol overnight at room temperature and

dark (all leaves should be inside alcohol). The next day, the resulting mixture with green color was filtered and blended with 250-300 mL hexane (the same amount of ethanol) and 5-10 mL of distilled water. In the n-hexane phase, the Chl-carotene and the dissolution of pigments in the water and ethanol phases were pulled away in 3 hours. Additionally, Chl and carotene were separated by adding silica gel to the n-hexane phase. After taking the top layer, 20-25 g of silica was added to the solution while mixing until the yellow color was achieved. Thirdly, the mixture was mixed at room temperature for 50 min. While doing filtration, the yellow liquid part was poured whereas keeping the silica in the beaker as much as possible. Then, the filtration process was conducted with 50-100 mL methanol, and the silica was washed at the same time until the silica lost its green color. Eventually, by using a rotary evaporator to evaporate the solvents, dark green and oily chlorophyll was produced. [62]

2.3.2 Synthesis of Red-Emitting Conjugated Oligomer (COL)

The monosaccharide functionalized conjugated oligomer synthesized in the previous study by our group was synthesized in the same way. [63] Briefly, red-emitting oligomers which carry azide groups were engaged for post-functionalized glycoconjugate oligomer synthesis. This functionalization was carried through a click reaction between azide groups and acylated mannose groups. 4,7-bis((E)-2-(9,9-bis(3- azidopropyl)- 9H-fluoren-2-yl) vinyl) benzo[c][1,2,5] thiadiazole (52.0mg, 60.0 μmol) and 2,3,4,6-Tetra-O-acetyl-O-prop-1-yl- α- D-mannopyranoside (92.7 mg, 240μmol) was put in 7 mL purged THF into a 25 mL round bottom flask. Then, the solution was stirred until completely dissolved for 10 min. In order to prepare aqueous solutions of $CuSO_4.5H_2O$ (6.00 mg, 24.0 µmol) and sodium ascorbate (9.51 mg, 48.0 μmol) separately, 1 mL degassed ddH_2O was used. After adding the $CuSO_4$ solution to the mixture, the ascorbate solution was added by using a pipette in order to add slowly while stirring the reaction solution and continued to mix at 50°C for 2 days. Then, the solvent was vaporized and the residual was washed by using water and waited until drying. Finally, the product

of pure red crystalline was obtained. (Figure 2.1)

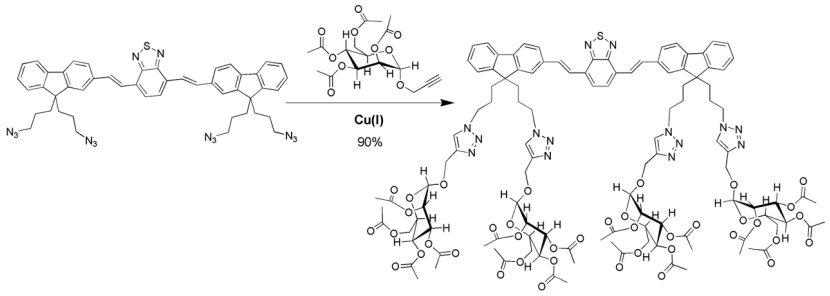

Figure 2.1: Schematic representation of 4,7-bis((E)-2-(9,9-bis(3- triazol- tetra-O-acetyl- α – D-mannopyranosyl)-9H-fluoren-2-yl)vinyl)benzo[c][1,2,5]thiadiazole synthesis. [63]

2.4 Reactive Oxygen Species (ROS) Detection

Light-induced reactive oxygen species (ROS) production capability of photosensitizers was investigated using a notorious 2,7-dichlorofluorescein diacetate (DCFH-DA) assay. Firstly, 2.5 mg of dichlorofluorescein diacetate (DCFH-DA) was solved in ethanol (5 mL). 500 μL was taken from this solution and added to 2 mL of 0.01 N NaOH, and stored at dark and room temperature (30 min). Then, 10 mL was taken from sodium phosphate buffer (PBS) and added to the solution, and stored in the fridge. With alkanaline media, dichlorofluorescein diacetate (DCFH-DA) was hydrolyzed and 40 μM solution of 2,7-dichlorofluorescein (DCFH) was obtained as depicted in Figure 2.2 The solution was stored in the dark and cold environment until usage.

First, the blank was measured (0 min). To do this, 500 μL of DCFH was added to a standard fluorescence cuvette and then 1mL of water was added to this solution, and after measurement, the wavelength of excitation and emission wavelength were obtained, 488 nm and 524 nm, respectively. Then, white light was applied to the solution with the intensity of 1 mW/cm^2 for a minute and the emission spectrum was obtained. This process was continued four times. So, the solution's emission intensity was obtained every minute for 4 minutes. After measuring blanks, 100 μL of 5 $\mu g/mL$ of each nanoparticle and 500 μL

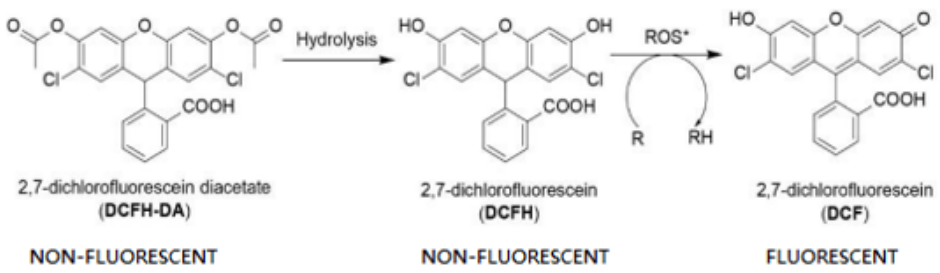

Figure 2.2: The detection mechanism of the DCFH-DA assay. The molecular structures of 2-7 Dichlorofluorescin diacetate (DCFH-DA), 2,7-dichlorofluorescein (DCFH), and with the reaction of ROS highly fluorescent 2,7-dichlorofluorescein (DCF) was produced.

of DCFH were taken and this solution was diluted by adding 1 ml of deionized water. An identical procedure was conducted to measure the ROS generation ability of nanoparticles.

2.5 Bacterial Experiments

2.5.1 Preparation of E. coli and B. subtilis Suspensions

A single colony of E.Coli and S. aureus were taken from semi-solid Luria-Bertani (LB) agar plate and put into a 15 ml flask with 5.0 mL of liquid LB culture medium. Then incubated (37°C, 200 rpm, 14 hours). Additionally, 10-20 μL of bacteria solution was placed in 15-20 μL of liquid LB medium and incubated at similar conditions. Centrifugation was used to harvest them (2 min, 4°C, 7000 rpm). After each centrifugation, bacterial solutions were washed with fresh 1X Phosphate buffered saline (PBS) at least four times in order to take away from both dead bacteria and LB medium. Then, the supernatant was discharged and bacterial residues were resuspended in PBS. While resuspending PBS was added to the solution by checking the optical density value at 600 nm (OD_{600}), and when the OD value was adjusted to $\sim$1.0.

2.5.2 Determination of Minimum Inhibitory Concentration (MIC Assay)

In order to determine the MIC values of nanoparticles, the broth microdilution method was followed after the preparation of bacterial suspension as described in subsection 2.5.1. Two different protocols were followed. Firstly, after the preparation of nanoparticles with different concentrations, 10 µL of each was taken and added to 100 μL of bacterial solution suspended in a 96-well plate. Two different protocols were followed. Firstly, after the preparation of nanoparticles with different concentrations, 10 μL of each was taken and added to 100 μL of bacterial solution suspended in a 96-well plate.

For the control group, 10 μL of Gibco 1X PBS was used. Then, the mixtures were incubated at 37°C for 1 hour. After that, the white light ($20mW/cm^2$) was applied to the both control and nanoparticle-treated groups. In the second protocol, bacteria were suspended in a liquid LB medium. Firstly, 2 mL of liquid LB was added to a 24-well plate, and 1 mL of stock nanoparticle was added to the first well and mixed properly. Then by taking 1 mL of solution from the previous well, was added to the next well and the last mL was thrown away. Finally, 50 μL of bacterial suspension was added to the solution. For the control group same process was conducted with 1X PBS. Similarly, after incubation for 1 hour, samples were exposed to light ($20mW/cm^2$). For the dark group, the same experiment was conducted. After that, both treated and non-treated groups were incubated (37°C, 100 rpm, 16 hours). Finally, by using a microplate reader OD_{600} values were obtained. In order to get smooth results, the experiments were replicated three times.

2.5.3 Antibacterial Activities of the Nanoparticles

2.0 mL of diluted bacterial suspensions were treated with distinctive concentrations of nanoparticles for 30 min (37°C, 200 rpm). Later, white light ($20mW/cm^2$) was irradiated to samples. The same experiment was carried out with the same

amount of PBS for the control group. 50 µL of 10^5-fold diluted bacterial suspensions were taken and spread on the LB agar plates and incubated for 64 h at 37°C. Colony forming units (CFUs) were measured following incubation. For the dark group, the same experiment was carried out without applying light. The decreasing graph of the mean log10 colony forming units (CFU) in accordance with exposing light and without light was drawn. Also, by using log_{10} reduction $= log_{10}(C/T)$ log reduction was evaluated (T and C indicate that control and treated groups).

2.5.4 Imaging of Antibacterial Activity by SEM

In order to remove organic contamination, silica wafers with the size of 1 cm x 1 cm were incubated in isopropanol and ethanol (30 min each). Then they placed at 37°C incubator to dry completely. 100 µL bacterial suspension having approximately 1 OD_{600} value was added to 1 mL of PBS, then these solutions were treated with each photosensitizer, and incubated in a shaker incubator at 37°C for 40 min. The white light was illuminated ($20mW/cm^2$). The same amount of PBS was used for the control groups, and for the dark group, the same procedure was carried out. 10 µL from each were placed onto silica wafers and fixed with 2.5% glutaraldehyde solution (in PBS) at 4°C for 14 h.

2.5.5 Agar Disk Diffusion Assay

The agar disk diffusion assay was conducted to evaluate the efficiency of antibacterial PDT of nanoparticles on E. coli and S. aureus bacteria. Both bacteria strains were suspended in liquid LB medium at 37°C, 200 rpm for 14 hours. Fresh LB was used to dilute bacterial suspension 100-fold and OD_{600} value was adjusted to 0.5–0.6 which is corresponded to the mid-log phase. 150 µL of bacterial solutions were taken and spread on agar plates. After incubation of 5 mm circular filter paper under UV light 10 µL of nanoparticles was poured to filter papers. For the comparison, the same amount of test antibiotic (ampicillin) was placed on filter

papers. After that, they were placed on the agar plates. After 10 min white light irradiation, agar plates were incubated at 37°C for 14 hours. After incubation, the nanoparticles' antibacterial activity was evaluated by measuring the radius of the inhibition zone.

2.6 In vitro Experiments

2.6.1 Cell culture

The appropriate medium that contains 88 % DMEM, 10 % fatal bovine serum, 1 % penicillin/streptomycin, 1% L-Glutamine, 0.1 mM non-essential amino acids, 1 mM sodium pyruvate was used to culture MCF-7 cells to T25 canted-neck tissue culture flasks and incubated at 37 $^{\circ}C$ with 5 % CO_2 - humidified and dark environment. After cells reached $\sim 70 - 80\%$ confluency, cells were transferred to T75 flasks by passaging. Then, continued to be grown by passaging each 3-4 days using Trypsin/EDTA solution.

2.6.2 Cytotoxicity and photo-cytotoxicity

In order to determine the dark- and photo-cytotoxicity of nanoparticles on mammalian cells in vitro, the methyl thiazolyl tetrazolium (MTT) assay was utilised. The MTT solution was prepared according to the code of the kid and stored at -20 $^{\circ}C$ in the dark until usage. The tetrazolium salt in the MTT experiment is converted to an insoluble formazan dye at 37 $^{\circ}C$ by the dehydrogenase enzyme that existed in viable cells (Figure (2.3)). Additionally, solubilizing agents are added to the insoluble formazan salt to dissolve it, and the colored result is quantitatively quantified at 570 nm using a spectroscopic micro-plate reader.

Tetrazolium salts can no longer be reduced by dead cells into colored formazan products. MTT is transformed into a purple formazan product with a peak

absorbance near 570 nm in viable cells with an active metabolism. As a result, the quantity of live cells in the culture directly correlates with the intensity of the colorful product.

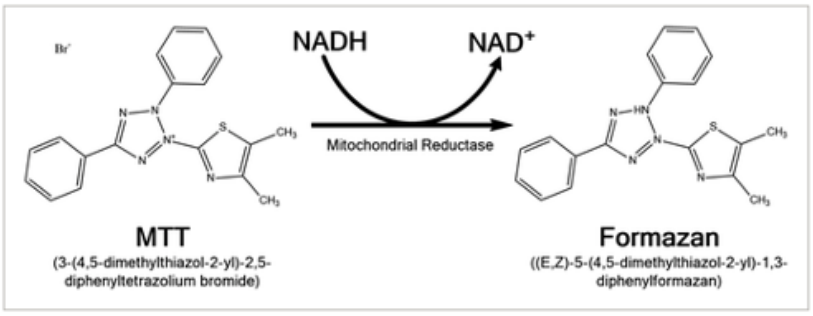

Figure 2.3: Reduction of MTT to formazan crystals. [64]

MCF-7 breast cancer cell line was engaged to conduct experiments. After calculating the cell density which is 4×10^3 cells/well, the cell suspensions were seeded onto 96-well plates with DMEM and incubated at $37°C$ in an incubator with 5% CO_2 for 24 h. After that, the cells were treated with different dosages of nanoparticles and incubated overnight. For the control group, the same amount of 1X Phosphate-Buffered Saline (PBS) was added and the same procedure was followed. While the white light ($20mW/cm^2$) was applied to nanoparticle-treated cells for 20 min for the determination of photo-cytotoxicity, the dark group was stored in the incubator. All groups were incubated overnight in a carbon dioxide incubator at 37 $°C$.

After 48h incubation, the medium was taken away, 100 μL of Gibco Dulbecco's Modified Eagle Medium (DMEM) and 10 μL of MTT with a concentration of 1.2 mM were added to well-plate and incubated for 4h at 37 $°C$. Later, the medium was aspirated and 110 μL dimethyl sulfoxide (DMSO) was added to wells to dissolve formazan crystals. After adding PBS, according to the number of living cells, the color change was observed. Finally, the cell viability of each cell was determined by reading absorbance values by a microplate reader at 570nm. The experiment was repeated four times for each concentration and for control groups.

Tables 2.1, 2.2, 2.3, and 2.4 provide the concentrations of nanoparticles used for MTT assay to measure relative cell viability (FC=Final Concentration, the

amount used from stock solution, FV/well=Final Volume for each well).

Table 2.1: Concentrations of COL used in MTT cell viability assays.

NPs Dark/Light	**FC(µM)**	**NPs(µL)**	**PBS(µL)**	**DMEM(µL)**	**FV/well(µL)**
Cell control	0	0	60	100	160
Conc.1	1.377	2	58	100	160
Conc.2	3.444	5	55	100	160
Conc.3	6.888	10	50	100	160
Conc.4	13.777	20	40	100	160
Conc.5	20.666	30	30	100	160
Conc.6	27.555	40	20	100	160
Conc.7	34.444	50	10	100	160
Conc.8	41.333	60	0	100	160

Table 2.2: Concentrations of COL-Au used in MTT cell viability assays.

NPs Dark/Light	**FC(µM)**	**NPs(µL)**	**PBS(µL)**	**DMEM(µL)**	**FV/well(µL)**
Cell control	0	0	60	100	160
Conc.1	1.344	2	58	100	160
Conc.2	3.444	5	55	100	160
Conc.3	6.722	10	50	100	160
Conc.4	13.444	20	40	100	160
Conc.5	20.166	30	30	100	160
Conc.6	26.888	40	20	100	160
Conc.7	33.611	50	10	100	160
Conc.8	40.333	60	0	100	160

2.6.3 Statistical Analysis

In accordance with the DMEM control group, MTT relative cell viability differences were normalized. The light and dark conditions analysis was carried out using a one-way analysis of variance (ANOVA). The data are emblematized as the mean ± Std. (n = 4) (** and **** demonstrate a great difference between groups with $p < 0.001$ and $p < 0.0001$, respectively)

2.6.4 CLSM Experiments

MCF-7 cells were cultured on treated 6-well tissue culture plates and microscope slides inside 6-well plates with a density of 4×10^5 per well in DMEM solution and

Table 2.3: Concentrations of Chl used in MTT cell viability assays.

NPs Dark/Light	**FC(µM)**	**NPs(µL)**	**PBS(µL)**	**DMEM(µL)**
Cell control	0	0	60	100
Conc.1	2.488	2	58	100
Conc.2	6.222	5	55	100
Conc.3	12.444	10	50	100
Conc.4	24.888	20	40	100
Conc.5	37.333	30	30	100
Conc.6	49.777	40	20	100
Conc.7	62.222	50	10	100
Conc.8	74.666	60	0	100

Table 2.4: Concentrations of Chl-Au used in MTT cell viability assays.

NPs Dark/Light	**FC(µM)**	**NPs(µL)**	**PBS(µL)**	**DMEM(µL)**
Cell control	0	0	60	100
Conc.1	2.166	2	58	100
Conc.2	5.416	5	55	100
Conc.3	10.83	10	50	100
Conc.4	24.888	20	40	100
Conc.5	21.66	30	30	100
Conc.6	32.5	40	20	100
Conc.7	54.166	50	10	100
Conc.8	65	60	0	100

incubated at $37°C$ for 24h. Then, 1 µM of four different nanoparticle groups which are Chl and Chl-Au, COL, and COL-Au were added to the culture, and the same amount of PBS was added for the non-treated control group. After being treated with nanoparticles, cells were incubated for 48h. After that, while white light is applied to the light group for 20 min, another group remained in incubation. The next day, firstly, the media was taken away, and cells were rinsed with PBS two times. Secondly, for the fixation process, 1mL 4 % paraformaldehyde solution was added and stored at $4°C$ for 10 min to acquire better fixation. The fixation solution was prepared by dilution of 37 % formaldehyde solution to 4 % by adding 1X PBS with a 1:9 ratio. Then, after aspirating the fixative solution cells were rinsed with PBS two times. After that, cells were permeabilized for 1 min in 0.1 % Triton X-100. Cells were thoroughly washed with PBS two times after aspirating the Triton. Then, one-two drop of DAPI solution was added and waited for 4 min, and the cells were observed at both Fluorescent and DIC Equipped Inverted Microscope and Leica Confocal Microscope.

Chapter 3

Results and Discussions

This chapter includes two sub-sections. Section 3.1 describes the preparation and characterization of red-emitting conjugated oligomer (COL) nanoparticles and their applications in anticancer therapy and cell imaging. In section 3.2, the characterization of chlorophyll and the preparation and characterization of chlorophyll nanoparticles are discussed. Moreover, photodynamic therapy applications were covered by displaying ROS generation ability.

3.1 Red-emitting Conjugated Oligomer (COL) Nanoparticles

The red-emitting conjugated oligomer (COL) nanoparticle and its hybrid conjugation with gold nanoparticles were synthesized through the nanoprecipitation method. The acetyl groups make it possible to manage the nanoparticles' size, increase their stability and enhance cell permeability via the hydrophobic effect. While the core of the oligomer is hydrophobic, side chains are hydrophilic. Therefore, by taking advantage of this, it is expected to achieve specific binding between mannose receptors and acetylated mannose groups in both bacteria and

mammalian cell walls. These water-dispersible nanoparticles demonstrated stability in an aqueous medium for prolonged times. Also, it is found that they show highly generation ability of reactive oxygen species (ROS). In this regard, these nanoparticles were investigated as a promising photosensitizer in antibacterial and anticancer photodynamic therapy (PDT) applications.

3.1.1 Preparation and Characterization COL and Hybrid Conjugated Gold (COL -Au) Nanoparticles

Soluble oligomers can be made dispersible in water by making nanoparticles using nanoprecipitation methods. A water-miscible solvent (i.e. THF, DMSO, DMF, etc.) like tetrahydrofuran (THF) that can dissolve the materials is utilized, and the solution (THF and oligomer) is injected onto the Milli-Q water drop by drop and ultrasonicated to hinder the aggregation and to promote dispersion, then after achieving a solution which is homogeneous, the solvent is evaporated. The preparation of nanoparticles is displayed in Figure 3.1.

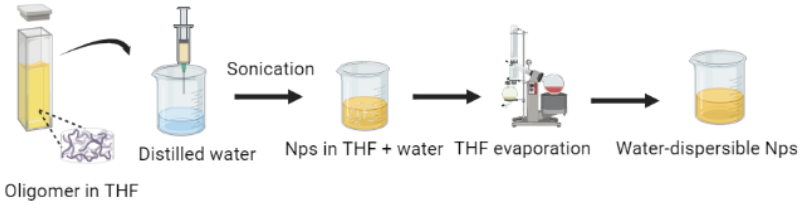

Figure 3.1: Preparation of conjugated oligomer (COL) nanoparticles by nanoprecipitation method.

Gold nanoparticles can be employed in photothermal therapy because they exhibit localized surface plasmon resonance (LSPR) in the near-infrared region of the electromagnetic spectrum. However, the results obtained from photothermal therapy were not successful. Therefore, since the higher ROS generation ability was obtained with hybrid conjugation with gold, the results were reported. In this regard, the same procedure was applied to prepare hybrid conjugated gold (COL -Au) nanoparticles after gold $AuCl_3$ was added to aqueous media (Figure 3.2).

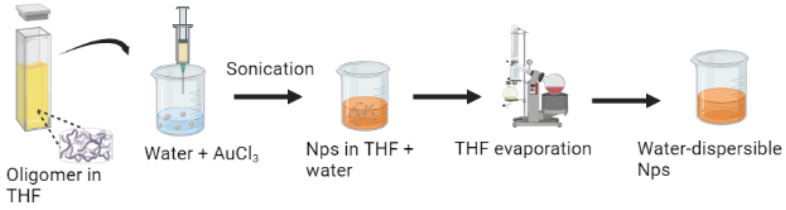

Figure 3.2: Preparation of hybrid nanoparticles of COL with gold nanoparticles by nanoprecipitation method.

In order to find an appropriate concentration of COL, 5 different solutions with distinctive concentrations from 1 mg/ml to 5 mg/ml were prepared, and DLS and zeta potential values were measured for moths. The most similar data with small changes were recorded for the concentration of 4 mg/ml. Therefore, this concentration was selected as an optimal concentration with around 115 nm hydrodynamic diameter, and whole experiments were conducted with this stock solution. The nanoparticles' zeta potential in water was +32.2 mV at $25°C$. The reason for this the positive $\zeta-$ potential is positive charges on the nanoparticles.

With the conjugation of gold nanoparticles, the hydrodynamic size of the nanoparticle is decreased to 100 nm. This is because the hydrophobic conjugated backbone oligomer folds around the $Au^{+}3$ ion, consequently encapsulating the gold. And also, there is a reduction in zeta potential owing to the fact that the surface area was diminished with the encapsulation of gold nanoparticles.

Table 3.1: Zeta potential and size values of solutions of COL and COL-Au nanoparticles.

Nanomaterial	**Size (nm)**	**Zeta-Potential (mV)**
COL	59,43	32,2
COL-Au	40,15	24,1

In order to evaluate the nanoparticles' stability in water, the hydrodynamic diameter and zeta potential values were measured and recorded for 30 days. As indicated in Figure 3.4, a remarkable change in the size of COL was not observed.

TEM and SEM were also used to analyze the morphology of COL and COL-Au.

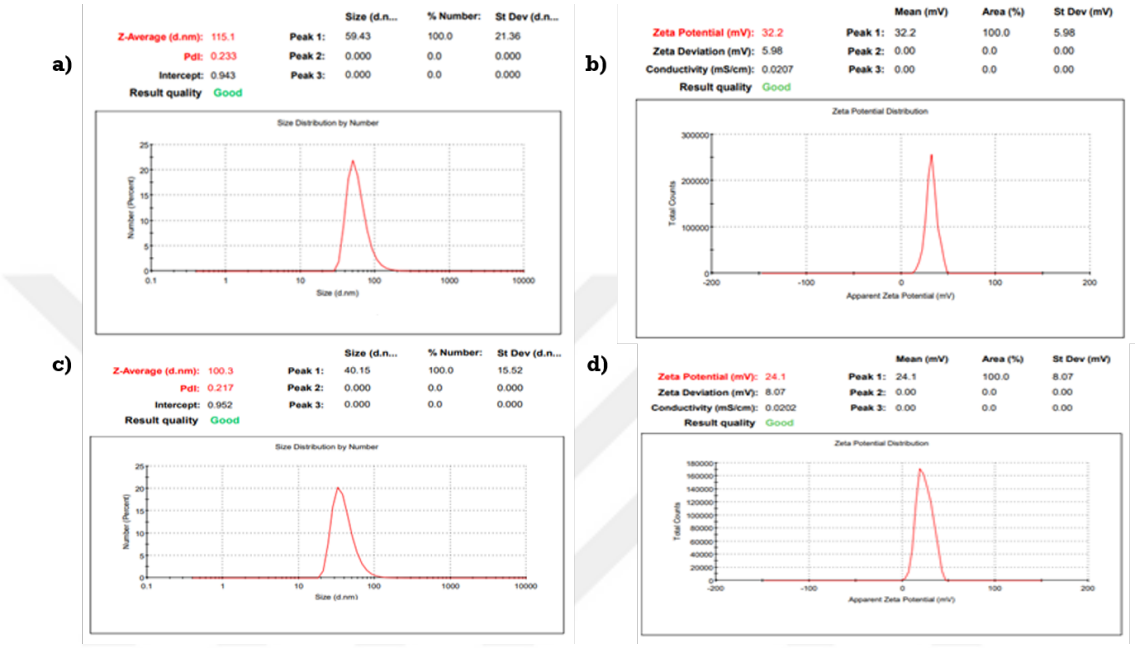

Figure 3.3: (a)DLS histograms of COL and COL-Au and (b) zeta potential values of COL and COL-Au, respectively.

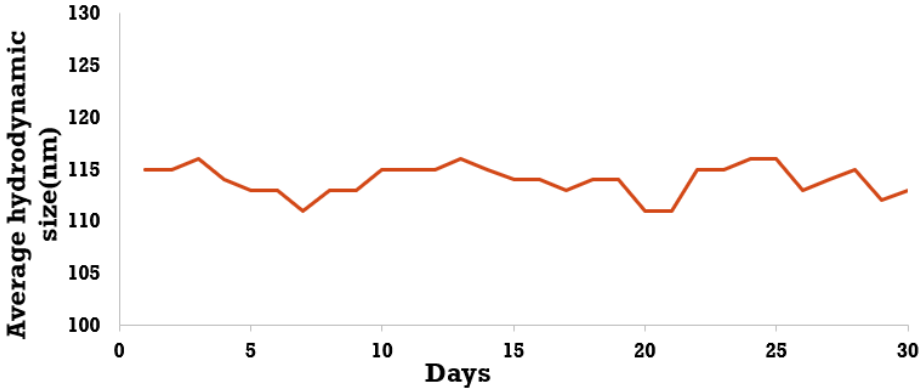

Figure 3.4: Average hydrophobic size distribution of COL in aqueous media.

The images obtained for both nanoparticles are not satisfying and the intended images could not be reported. According to SEM and TEM images represented in Figure 3.5, COL has a spherical shape with different sizes, and small clustered particles are also observed for both COL and COL-Au nanoparticles. In Figure 3.5c, the grey parts indicate nanoparticle solution and the shiny parts display gold nanoparticles. This means that the gold nanoparticles were encapsulated by conjugated oligomer properly without causing agglomeration.

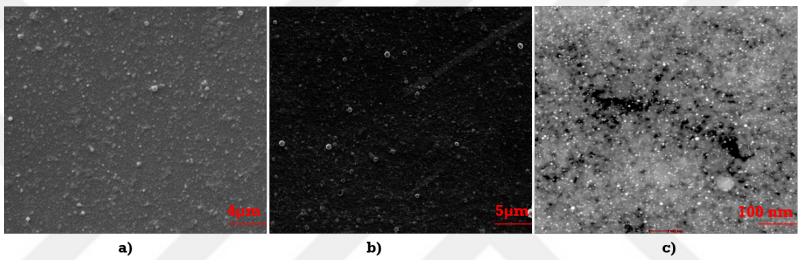

Figure 3.5: (a) SEM image of COL (b) SEM image of COL-Au and (c) TEM image of COL-Au.

3.1.2 Photophysical Properties and ROS Generation Ability of COL and COL-Au Nanoparticles

The photophysical characteristics of COL and COL-Au were evaluated using UV-VIS-NIR absorbance and fluorescence spectroscopy. Absorption peaks for COL and COL-Au were recorded at 369 nm and 480 nm respectively. The difference between absorbance values is explained by the strong absorption capability of colloidal solution which is gold in the visible spectrum. It can be said that the results were obtained as expected when the results were compared with the study in which conjugation red-emitting conjugated oligomer with amine groups in the pendant chain with the gold nanoparticle. [48] Likewise, Timuçin Balkan et all. synthesized hybrid conjugated oligomer with tertiary alkyl amine side chains -silver nanoparticles (AgNPs) and reported UV-Vis absorption spectra among the different concentrations. Similarly, the specific peak for Ag nanoparticles was only obtained with higher Ag concentrations which can support to results obtained in this study. [65] As illustrated in Figure 3.6, COL has an emission

peak centered at around 605 nm, and 607 nm excitation wavelength was recorded for COL-Au.

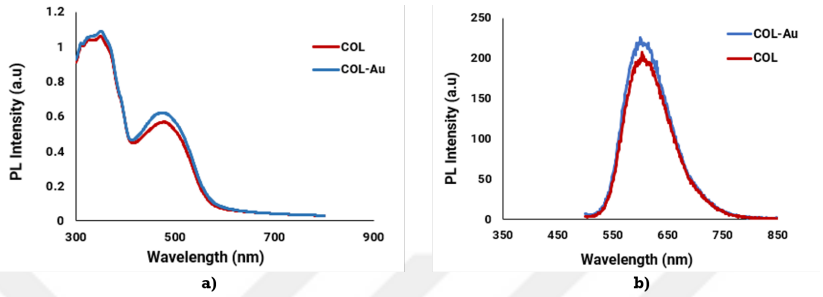

Figure 3.6: The absorption (a) and emission (b) spectral diagram of COL and COL-Au.

By using the DCFH-DA assay as explained in Section 2.4 the ROS production capabilities of COL and COL-Au were measured under white light ($1mW/cm^2$) exposure and the recorded results are displayed in Figure 3.7.

For COL, the intensity of fluorescence emission rise to 300 nm in a minute and proceed to increase, reaching nearly 800 nm when lighten for four minutes. The fluorescence emission intensity of COL-Au is about 300 nm within a minute and continued to increase, approaching nearly 1000 nm when irradiated for five minutes. These results indicate that COL and COL-Au can produce ROS considerably even with a small dosage of white light ($1W/cm^2$). The reason for the higher emission intensity for COL-Au is explained by the metal-enhanced ROS production effect.

The light-activated ROS production ability of COL and COL-Au, and DCFH oxidation of blank have shown a continuous raise in the peak intensity with the application of white light. For COL, the fluorescence emission intensity increased to around 300 nm in a moment and continued to ascend, approaching approximately 800 nm when exposed for four minutes. For COL-Au, the fluorescence emission intensity increased to about 300 nm in a minute and rise continually, reaching roughly 1000 nm when exposed for five minutes. These results indicate that COL and COL-Au can produce ROS significantly even though at a low dosage of white light ($1W/cm^2$).

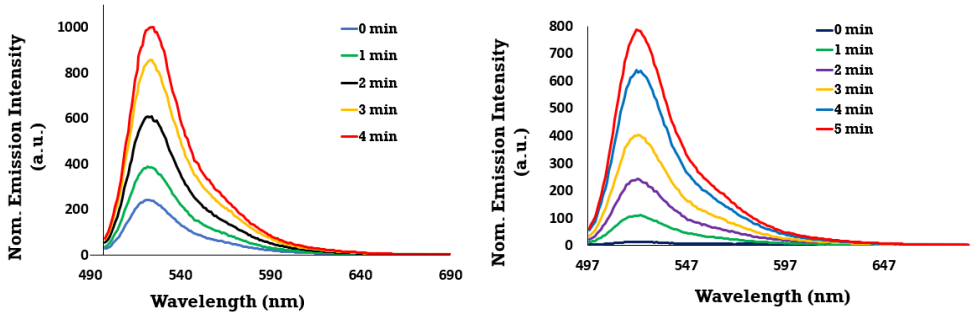

(a) (b)

Figure 3.7: a) Fluorescence intensity of DCF at 524 nm which is blank and COL under continuous white light exposure. b) The ROS measurement result for COL-Au.

3.1.3 Examination of Cytotoxicity and Phototoxicity of COL and COL-Au Nanoparticles on E. coli and S. aureus

After confirmation of the ROS generation abilities of nanoparticles, the biocidal activity of them under light irradiation was analyzed against E. coli (Gram-negative) and S. aureus (Gram-positive). Antibacterial experiments were studied in the dark and under white light illumination with a flux of $20 mW/cm^2$ by performing the surface plating method (Figure 3.8). According to the results, both COL and COL-Au did not show significant dark toxicity while they display light-induced killing effects toward bacteria. Additionally, the agar disk diffusion assay was conducted in the dark and with light exposure for 20 min. Figure 3.9). compares the plate images from the agar disk diffusion assay with the corresponding graphs of the inhibition zone radius for nanoparticles and ampicillin against E. coli. According to the findings of the agar disk diffusion method, ampicillin had an inhibition zone radius of approximately 7 mm both in the dark and under light conditions. For the COL and COL-Au nanoparticles, the inhibition zone radius was measured as 4 mm and 5 mm, respectively. Since the nanoparticles have high reactive oxygen species production ability, it is expected to be an additional treatment method to antibiotics with displaying high killing efficiency with light illumination. Nevertheless, the killing efficiency is not high

as expected, remaining nearly a 5 mm inhibition zone. The reason for this is the unsuccessful interaction between nanoparticles and bacterial cell walls. Despite the fact that higher interactions were achieved by gold nanoparticle conjugation, the phototoxicity of nanoparticles has remained at low efficiency. Furthermore, when it is compared with the oligomer with different functional groups, which have similar characterization results, this nanomaterial had an inhibition zone of almost 7 mm, while the result for COL-Au nanomaterial remained at 4.7 mm [48]. As stated earlier, the main reason for this is that the desired connection with the cell cannot be achieved. Also, the SEM images prove that these nanoparticles cluster in PBS and LB solution onto the bacteria cell wall (Figure 3.10).

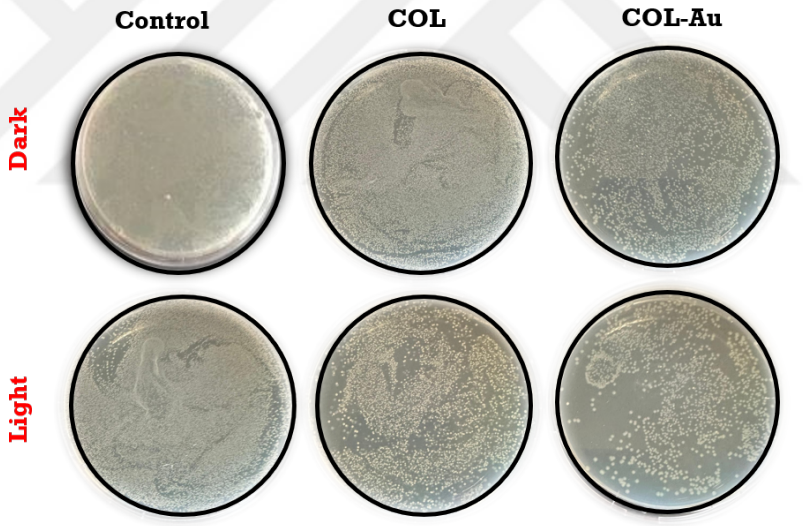

Figure 3.8: Agar plate photographs for E. coli on agar plate treated with nanoparticles and non-treated control in the dark and with light exposure.

3.1.4 Examination of Mammalian Cancer Cell Cytotoxicity and Photocytotoxicity of COL and COL-Au Nanoparticles

MTT assay was utilized for the evaluation of the cytotoxicity of nanoparticles on mammalian cells in-vitro by using the most used breast cancer cell line, MCF-7. Different amounts of COL and COL-Au were incubated with MCF-7 cell lines

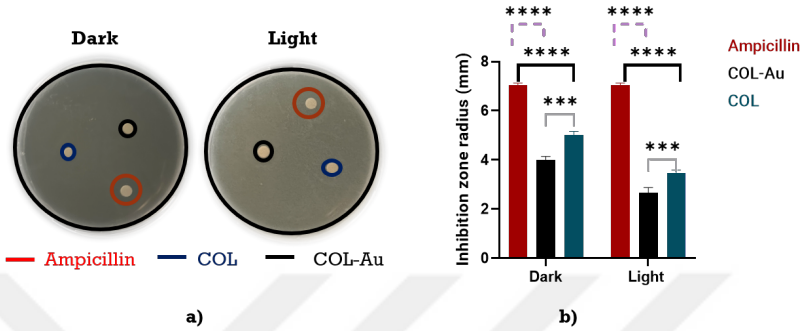

Figure 3.9: a) Agar disk diffusion assay plate photographs of COL and COL-Au nanoparticles towards E. coli (indicated with blue and black) and ampicillin (indicated with red) in the dark and under light illumination. b) The corresponding radius of the inhibition zone graph of E. coli. Multiple paired t-test was performed to compare results for the significant differences between groups. (*** and **** indicate a significant difference between groups with $p < 0.001$ and $p < 0.0001$, respectively).

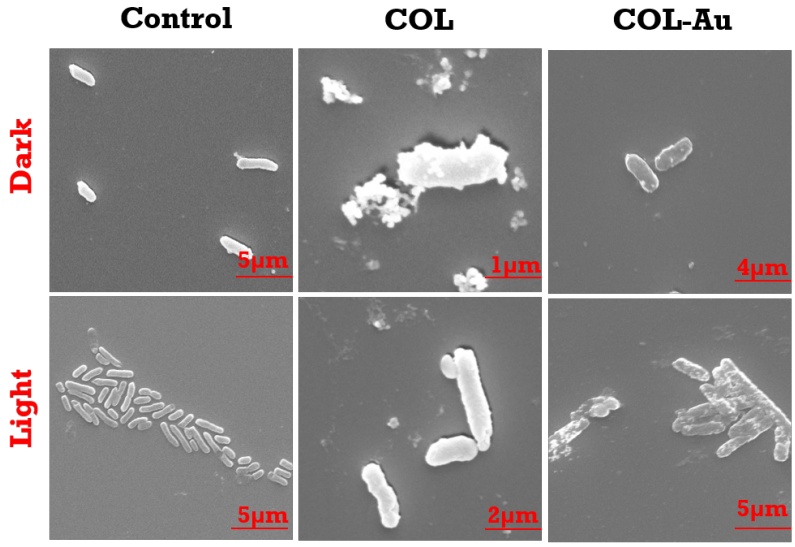

Figure 3.10: SEM images of E. coli treated with COL and COL-Au and non-treated in the dark and under white light illumination ($20mW/cm^2$) for 20 min.

in dark and under light exposure. In order to investigate the dark cytotoxicity of COL and COL-Au, different concentrations from 1.37 to 41.3 µM, and from 1.34 to 33.61 µM were used, and for control groups, the same procedure was applied with PBS. At lower concentrations, both COL and COL-Au did not show significant cytotoxicity on MCF-7 cells, but by adding 40 µL of each nanoparticle a decrease in relative cell viability was observed. The photodynamic efficiency of nanoparticles was examined by white light ($20mW/cm^2$) illumination to MCF-7 cells for 20 min. By contrast with the dark case, a significant reduction in relative cell viability was recorded with light irradiation, and along with these results, the activation of nanoparticles with light is proved. As seen in Figure 3.11, when we compare samples treated with nanoparticles and the control group, a remarkable reduction was seen even with 1.377 µM of COL ($p < 0.0007$). Similar results were observed for the MCF-7 cells treated with COL-Au with a higher reduction in cell viability ($p < 0.0001$). Consequently, the reduction in cell viability was reported for both nanoparticles even at low concentrations. According to these results, it can be deduced that the PDT efficiency of the COL at a similar concentration was improved by the conjugation of Au nanoparticles and COL.

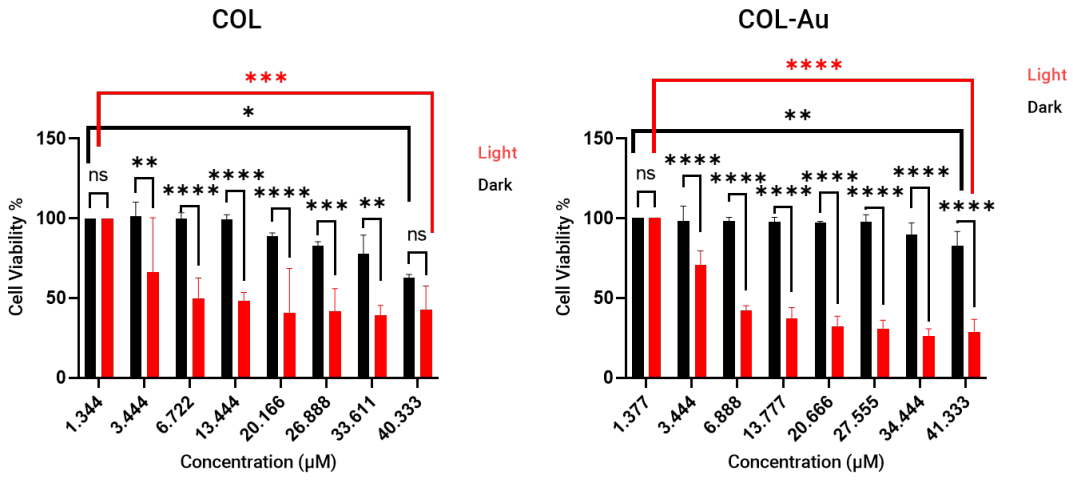

Figure 3.11: Relative cell viability (%) of COL and COL-Au against MCF-7 breast cancer cells at various concentrations ate dark and light irradiation ($20mW/cm^2$, 20 minutes). 2-way ANOVA multiple comparison tests were conducted to compare results for the notable differences between groups. (** and **** demonstrate a considerable difference between groups with $p < 0.0011$ and $p < 0.0001$,respectively).

3.1.5 Cellular Imaging by COL and COL-Au Nanoparticles

By using the MTT assay, NPs' photodynamic anti-cancer effect was demonstrated on the MCF-7 cell line. Along with the results of the MTT assay, in addition, the results and interaction between cells and NPs were approved with confocal laser scanning microscopy (CLSM), and cellular imaging application was examined. As the NPs have fluorescence properties by nature, they can be favorable to use directly for cellular imaging or image-guided PDT for cancer treatment. Confocal laser scanning microscopy (CLSM) was used to compare NP-treated and untreated cells to determine whether or not NPs may be absorbed by MCF-7 cells, as shown in Figure 3.12. After 21h incubation of cells on microscope slides, they were treated with 6.2 µM of NPs for 72 h. Moreover, the white light was applied for 20 min to light groups. Then, by adding DAPI nucleus of the cells was stained. When excited by a 461 nm laser, DAPI produces blue fluorescence emission, whereas COL-Au produces red fluorescence when excited by a 480 nm laser. As proven in Figure 3.12, the cellular uptake of COL-Au was concentrated primarily surrounding the nuclear membrane.

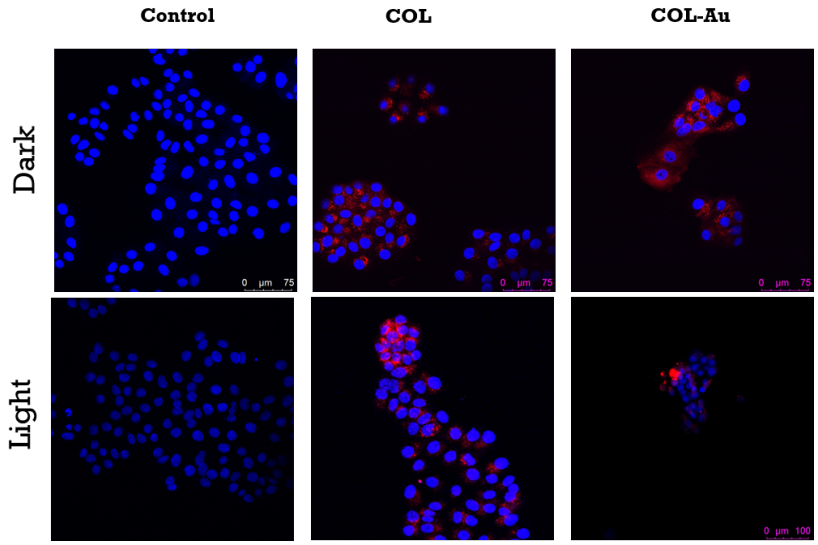

Figure 3.12: CLSM images of non-treated MCF-7 cells, COL-treated cells and COL-Au-treated cells.

3.2 Chlorophyll and Chlorophyll Nanoparticle

3.2.1 Characterization of Chlorophyll

The chlorophyll was obtained by following the procedure indicated in Section 2.3.1, as shown in Figure 3.13.

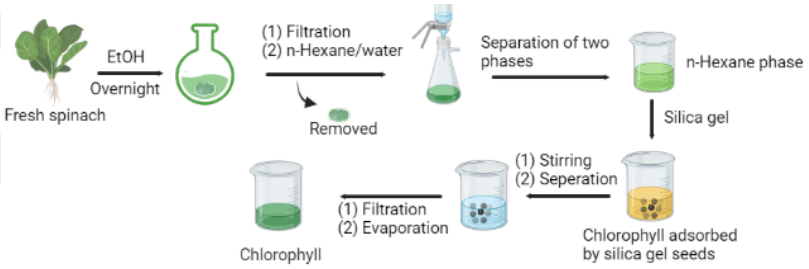

Figure 3.13: Schematic display of the extraction of chlorophyll from spinach leaf.

Extracted chlorophyll contains a mixture of chlorophyll a and chlorophyll b and a minor amount of pheophytin a and pheophytin b. (Figure 3.14) Chlorophyll is made up of four pyrrole rings that are linked together structurally by a magnesium ion and a long hydrophobic alkyl chain. The difference between chlorophyll a and chlorophyll b is the functional group. While chlorophyll a has a methyl group (-CH_3), chlorophyll b has a formyl group (-CHO). Moreover, pheophytin a and b are oxidation products of chlorophyll (Mg in the center is gone).

Figure 3.15 displays the FT-IR spectra of the spectral interval within the 4000-400 cm^{-1} wave band. FTIR spectra showed the vibration functional group C-H_3 and C-H_2 of chlorophyll around 2920 cm-1 and 2850 cm^{-1}, respectively. Moreover, chlorophyll revealed broad adsorption centralized at 3400 cm^{-1} for its hydroxyl group. The appearance of a strong peak at 1735 cm^{-1} account for the vibration of the ester group C=O. Additionally, the C-N vibration of porphyrins at 1644 cm^{-1} and the C-O vibration at 1045 cm^{-1} were recorded. When the results were compared with the literature spectra, the main peaks obtained from functional groups are similar only with a small difference that is caused by the type of the plant and the procedure used to extract [67]. Also, it can be said that chlorophyll is extracted successfully since there is a high overlapping with

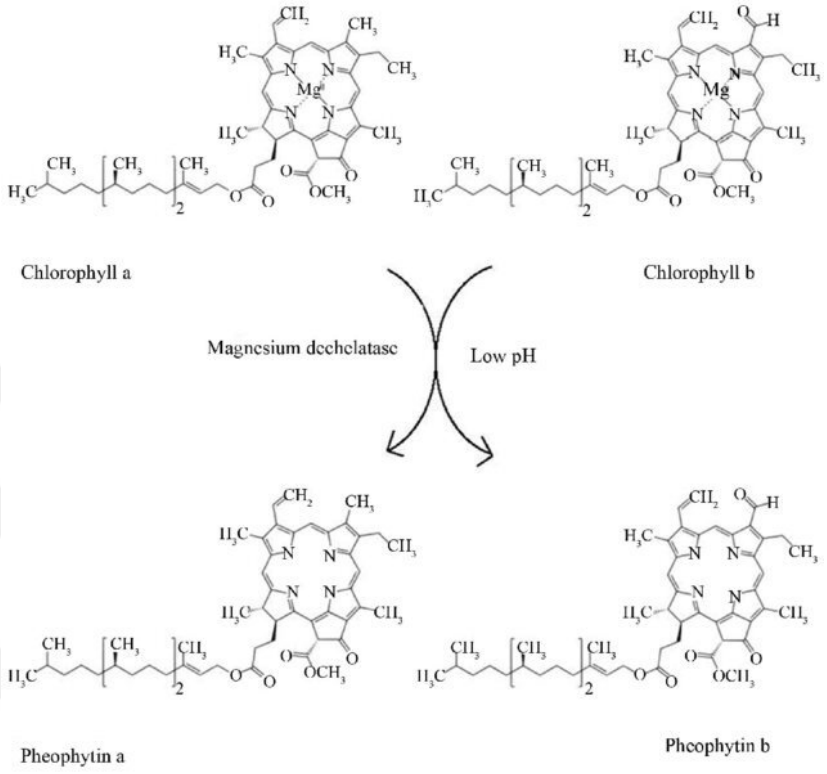

Figure 3.14: The chemical structure of Chlorophyll a, Pheophytin a, Chlorophyll b, Pheophytin b. [66]

peaks of literature spectra.

The ESI-MS spectra showed the presence of both chlorophyll a (Ma) and chlorophyll b (Mb) in the final product with their molecular weight, Ma: $C_{55}H_{72}O_5N_4Mg$, and Mb: $C_{55}H_{70}MgN_4O_6$ respectively.

After proving the presence of both chlorophyll a (Ma) and chlorophyll b (Mb) in the final product with their molecular weight by mass spectroscopy. The following confirmation was performed by ^{1}H-NMR spectroscopy and is shown in Figure 3.16. In Figure 3.17, a triplet of an olefinic proton is seen at 5.31 ppm, and so assigned to P2. Two multiplets are seen at 4.50 ppm (1H) and 4.47 (2H). The former couples with the doublet of the methyl group give a peak at 1.74 ppm, and this is assigned to H-4. The signal at 4.14 ppm (1H) is attributed to H-3 because it couples with a multiplet at 2.39 ppm. The signal of a methyl group at 1.73 ppm interacts with a multiplet from two protons at 3.79 ppm. The

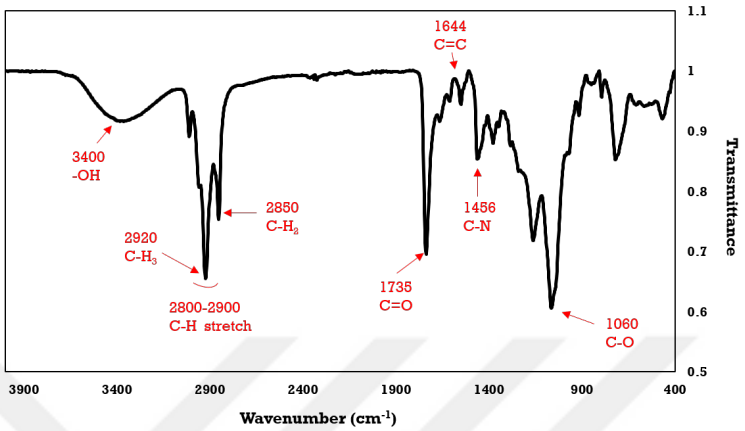

Figure 3.15: FT-IR spectra of chlorophyll.

ethyl group on C-8 is responsible for these resonances. At 3.8 ppm, 3.50 ppm and 3.3 ppm, and 3.2 ppm four methyl group signals appear as singlets and are assigned to 21, 18^1, 8^1, and 13^1 respectively. The reason for this can be set out by the chemical shift of the carbon atom, and attributed to methoxy group H-21. The chemical shifts belonging to the other three molecules are located on a double bond. A proton multiplet at 2.6 ppm and 2.315 ppm belongs to the same C-atom and is assigned to the H-3^1. Equivalently, the multiplets at 2.3 ppm and 2,089 ppm are related to the same C-atom and are allocated to the H-3^2 protons. The allylic methylene group and methylene group in Phytane are recorded with a multiplet at 1.9 ppm and 1.29 ppm. Lastly, the solvent peak is seen at 7.269 ppm. Although ^{1}H-NMR spectrum is not pure, when main peaks were compared to the literature, the results show that the extraction is accomplished successfully.

3.2.2 Preparation and Characterization of Chl and Chl-Au Nanoparticles

Chlorophyll nanoparticles were prepared by conducting the same procedure used to prepare conjugated oligomer nanoparticles.

As depicted in Figure 3.18, the hydrodynamic diameter of Chl NPs was

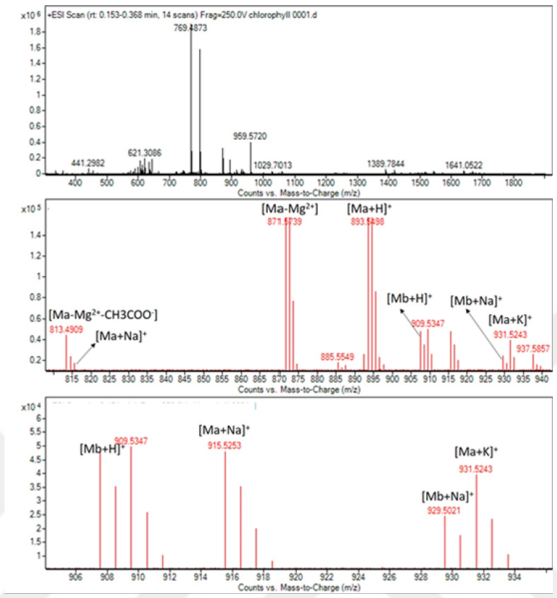

(a)

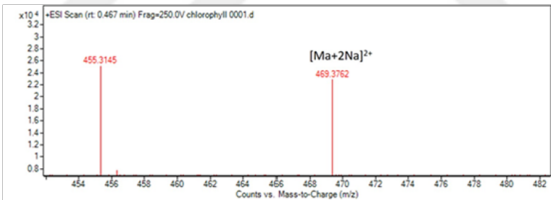

(b)

Figure 3.16: ESI-MS spectra of the corresponding chlorophyll a and chlorophyll b.

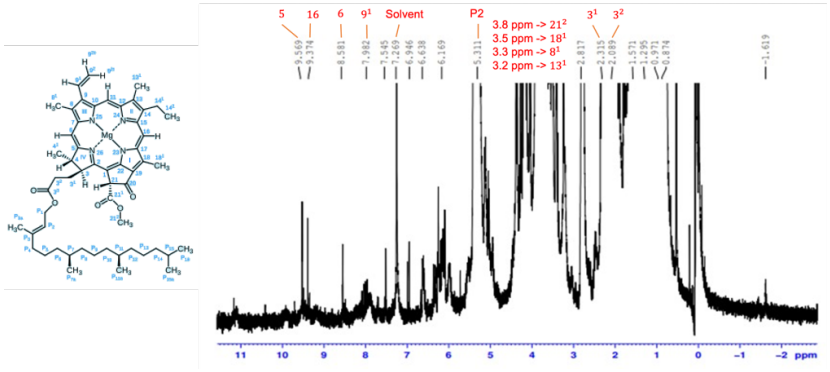

Figure 3.17: ^{1}H-NMR of chlorophyll (400 MHz, $CDCl_3$, 25 ^{o}C).

recorded at around 80 nm. On the other hand, the zeta potential of the Chl nanoparticle in water was -43.1 mV at $25°C$. The reason for the negative $\zeta-$potential is negative charges on the nanoparticles.

Similarly, as the chlorophyll was conjugated with gold, Chl-Au NPs were recorded to have a hydrodynamic diameter at around 88.27 nm, and the measured zeta potential value is -50 mV. Shaimaa Alexeree et. al reported that chlorophyll b is negatively charged and the zeta potential value of chlorophyll b - gold nanoparticle conjugation is around nearly -30 mV [52]. However, the zeta potential of chlorophyll conjugation with gold nanoparticles was measured as approximately -51 mV because extracted chlorophyll contains both Chl a and Chl b. The gold nanoparticle binds the magnesium ion at the center of Chl a and increases the surface area and negative charges, gold nanoparticle makes a connection with Chl b through the formyl group and is so encapsulated by Chl b.

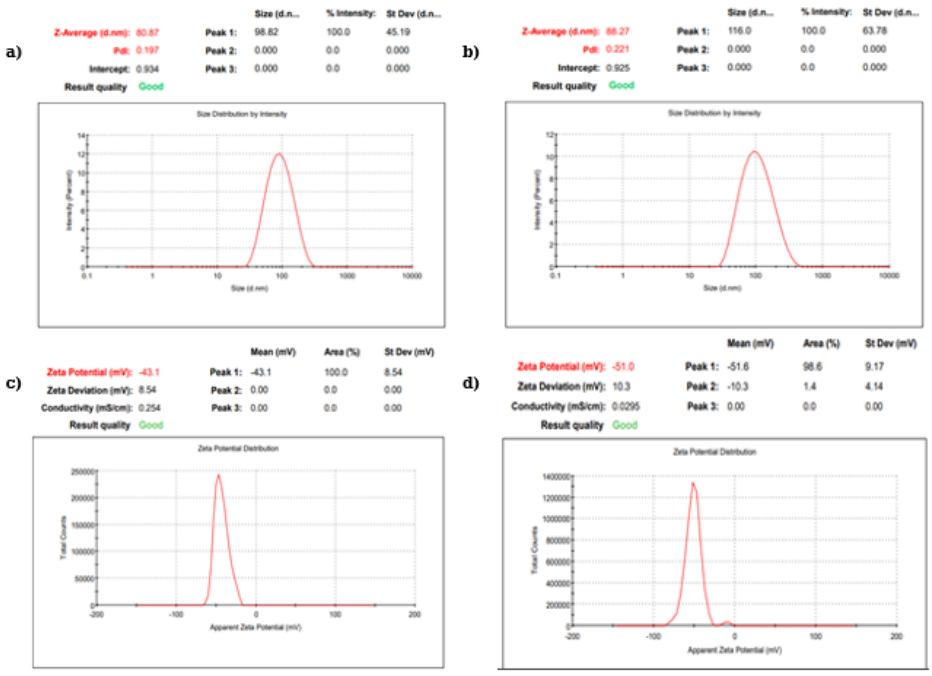

Figure 3.18: a) DLS histogram of CHL, b) DLS histogram of CHL, c) Zeta measurement result of CHL d) Zeta potential value of CHL-Au.

The stability of Chl and Chl-Au Nps in water was evaluated by measuring

zeta values and hydrodynamic sizes for 30 days. The results revealed that the nanoparticles can maintain their stability in aqueous media for quite a long time, as displayed in Figure 3.19.

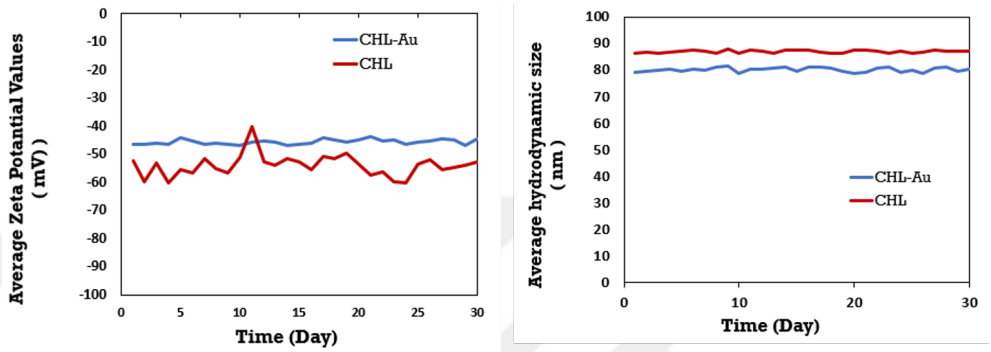

Figure 3.19: (a) Average hydrophobic size distribution and (b) Average zeta potential values of Chl and Chl-Au in aqueous media for 30 days.

TEM and SEM were also used to analyze the morphology of Chl and Chl-Au. The TEM images obtained for both nanoparticles are not satisfying and the intended images could not be reported. According to SEM and TEM images represented in Figure 3.20, chlorophyll has a spherelike and four-leaf clover shape with different sizes. In Figure 3.20d, the grey parts indicate nanoparticle solution and the shiny parts display gold nanoparticles. This means that the gold nanoparticles were encapsulated by chlorophyll properly without causing agglomeration.

3.2.3 Photophysical Properties and ROS Generation Ability of Chl and Chl-Au Nanoparticles

Figure 3.21 displays the absorption spectra of Chl and Chl-NPs nanoparticles. The main absorption peaks are the intense Soret band (B-bands) of Chl at about 415 nm and 453 nm. The O-bands, absorption value of the ground state to the first state transition, is around 642 nm and 670 nm. Similarly, both B-bands and Q-bands of Chl are maintained for Chl-Au NP. On the other hand, the peak at around 530 - 550 nm is characteristic of the gold nanoparticles' surface plasmon

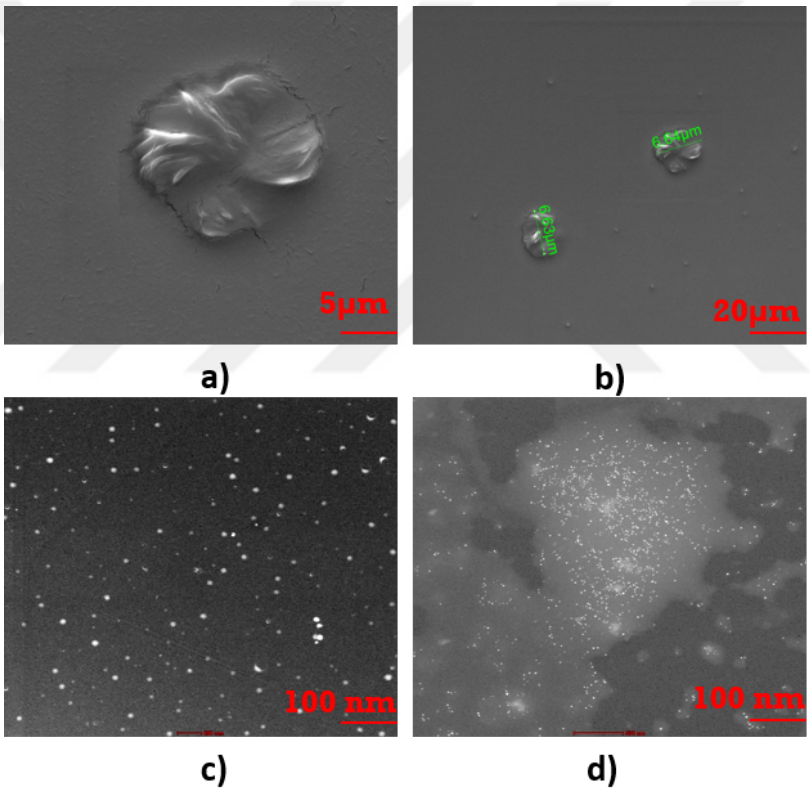

Figure 3.20: SEM images of (a), (b) chlorophyll and TEM images of (c) Chl and (d) Chl-Au nanoparticles.

resonance. Vito Rizzi et all. examined photoactivity and photostability of chlorophyll a, and reported that chlorophyll a nanoparticle has two absorption peaks at 417 nm and 662 nm [68]. Similarly, Shaimaa Alexeree et all. studied photodynamic therapy applications of chlorophyll b-gold nanoconjugate, and reported that chlorophyll b has 4 main absorption peaks at around 415 nm and 453 nm with high intensity and 642 nm and 670 nm with lower intensity [52]. Moreover, in both of the studies, the characteristic absorption peak of Au nanoparticles was measured at around 520 nm. With the comparison of literature and extracted chlorophyll, the extraction was held successfully and both chlorophyll a and chlorophyll b give main peaks clearly.

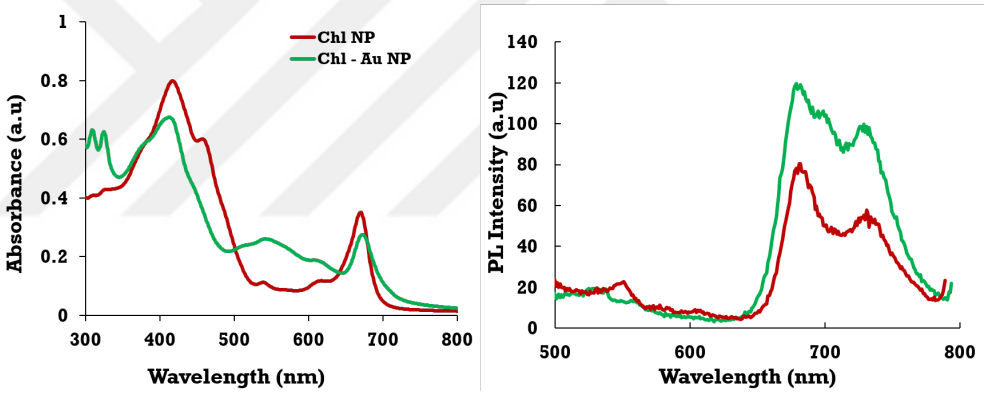

Figure 3.21: UV-vis absorbance and fluorescence emission spectrum of chlorophyll-based nanoparticles.

Since fluorescence emission value depends on the absorption wavelength, the measured absorbance values were used to excite nanoparticles. The chlorophyll fluorescence emission spectrum ranges from 640 nm to 750 nm; has two apparent peaks in the red region at around 680 – 690 nm and in the far-red region between 700 and 740 nm. These peaks can be observed for both Chl NP and Chl-Au NP, when the nanoparticles were put under the excitation of 407 nm and 404 nm, respectively. The indication of gold is believed to be around an emission wavelength of 550 nm, which can be seen from these Chl-Au NPs. Even at a lower intensity, this nanoparticle is still able to produce emissions in the red region at around 680 nm and in the far red at 730, attributed to the presence of chlorophyll. As reported in the literature previously, the fluorescence emission spectrum of chlorophyll b - gold nanoparticle conjugation was measured in the red region

at around 682 nm and in the far-red region at 745 nm [52]. Moreover, the fluorescence emission spectrum chlorophyll a - gold nanoparticle conjugation has two main peaks at 667 nm and 725 nm [68]. According to these studies, the obtained fluorescence and absorbance values of the prepared chlorophyll nanoparticle and chlorophyll with gold conjugation were similar to the literature that promotes successful results.

It is commonly known that chlorophyll has relatively long-living excited states and is quite effective at absorbing light. In the presence of light, singlet chlorophyll that has been excited directly results in the creation of the highly reactive triplet chlorophyll. In this regard, the Chl-NP and Chl-Au NP efficiency of ROS generation under white light illumination ($1mW/cm^2$) was carried out using the DCFH-DA assay. As the 2,7-dichlorofluorescein (DCFH) was exposed, a very weak emission peak was obtained at 524 nm due to the auto-oxidation of DCFH to DCF. The addition of nanoparticles to the solution has caused illumination to produce the peak intensity at 524 nm with significant raise and continued to increase progressively over the lighting period. These results proved that both Chl-NP and Chl-Au NP have the potential as photosensitizers with fairly high ROS generation capability just under the small flux of white light. Comparing the ROS production capabilities of Chl-NP and Chl-Au NP, higher photoluminescence intensity was recorded and with the exposure of light, the redshift was observed. This might be attributed to the effect of metal-enhanced ROS generation of gold nanoparticles, a raise in intra-and interchain reactions, high order aggregation, and effective energy transfer to lower energy emitting states. The light-activated ROS production ability of Chl and Chl-Au, and DCFH oxidation of blank have shown a continuous raise in the peak intensity with the application of white light, and the peak intensity hit approximately 900 and 1000 for Chl and Chl-Au. These results indicate that these nanoparticles display notable light-activated ROS generation capability (Figure 3.22).

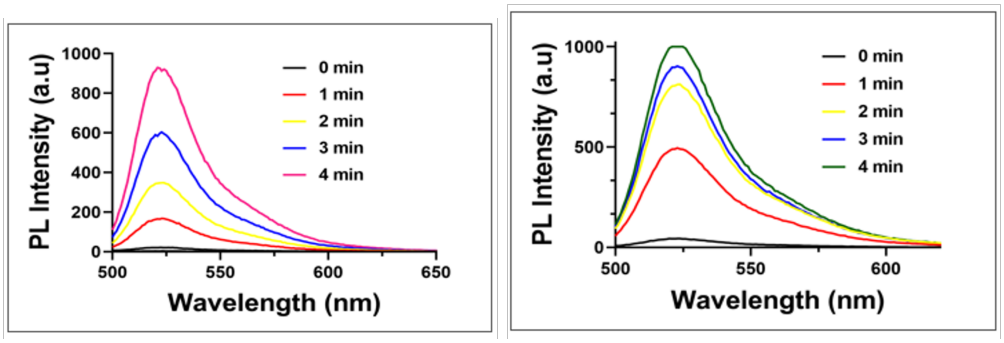

(a) (b)

Figure 3.22: (a) Fluorescence spectra of DCF at 524 nm for Chl NP under white light. (b) Fluorescence spectra of DCF at 524 nm for Chl-Au NP under white light.

3.2.4 Examination of Cytotoxicity and Phototoxicity of Chl and Chl-Au Nanoparticles on E. coli and S. aureus

Following the discovery that Chl and Chl-Au nanoparticles have a large yield of ROS production, their light-induced biocidal activity was investigated. Since gram-negative bacteria are responsible for the vast majority of infectious diseases, they were selected as a representative organism for this reason. S. aureus (a gram-positive bacteria) was also taken into consideration in order to qualify nanoparticles as a broad-spectrum antibacterial agent. The interactions between nanoparticles and S.aureus and E. coli were investigated.

Firstly, the minimum inhibitory concentration (MIC) value was established in the dark and under white light exposure with a flux of $20mW/cm^2$ treating E. coli with concentrations varying from 2.21 µM to 20 µM and from 1.19 µM to 17 µM in order to determine the best concentration range of Chl and Chl-Au for the inactivation of E. coli, respectively. Their optical density at 600 nm ((OD_{600})) was recorded after the nanoparticle-treated bacteria and the non-treated control group were maintained in both light and darkness. Information regarding the development of microorganisms is derived from the (OD_{600}) data. It is a sort of turbidity measurement that uses an absorbance detection method to quantify

scattered light. More light will be dispersed by the bacteria the more there are in the solution. The lowest concentration of an antimicrobial agent that prevents microorganisms from growing visibly is known as the MIC value. According to the MIC determination study, there is not any significant difference in the effect of different dosages of nanoparticles against E. coli in the dark. On the other hand, the data under photoirradiation showed that the antimicrobial effectiveness was improved by light illumination. Although the OD values were decreased to 0.569 nm and 0.427 nm by treating with Chl and Chl-Au, a more progressive reduction has been expected with increasing concentration. (Figure 3.23)

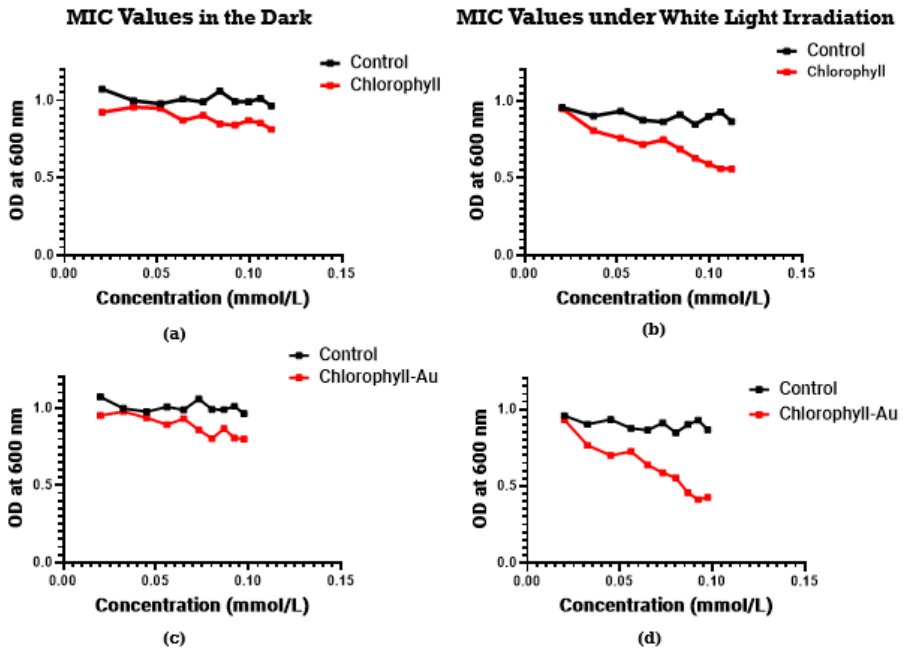

Figure 3.23: MIC assay of Chlorophyll-Au (a) in the dark and (b) under the white light and MIC assay of Chlorophyll (c) in the dark and (d) under white light exposure in comparison to the control groups.

After estimating the possible MIC value which is 8.60 µM for Chl and 7.49 µM FOR Chl-Au, the nanoparticle's photodynamic antibacterial activity was studied in darkness and with light illumination using the surface plating method. The colony forming unit (CFU) values were calculated and shown in Figure. With 20 min light exposure, the reduction from 7.6 to 7.1 and 6.91 for Chl and Chl-Au was recorded and shown in Figure 3.24. However, in the dark the reduction is small. Although nanoparticles have a killing effect on bacteria, the results were

not as expected. The reason for this might be the poor solubility of chlorophyll in aqueous media.

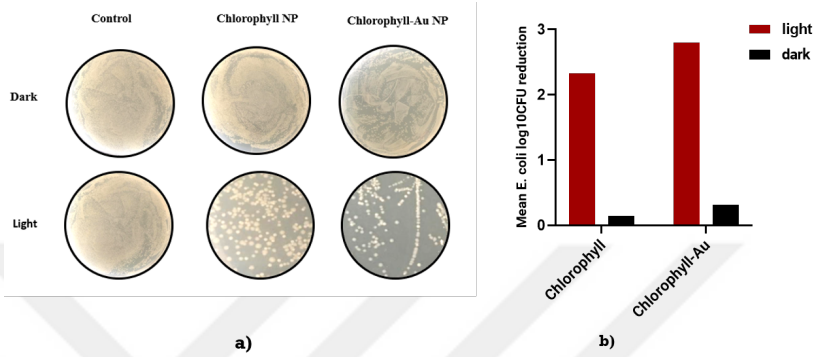

Figure 3.24: a) Agar plate images for E. coli treated with nanoparticles and non-treated control in the dark and under light b) Bacterial killing performance of nanoparticles toward E. coli under light exposure.

Additionally, in order to analyze the further photodynamic antibacterial activity of nanoparticles the agar disk diffusion assay was conducted in the dark and with light exposure for 20 min. Figure 3.25 compares the plate images from the agar disk diffusion assay with the accounting for graphs of the inhibition zone radius for nanoparticles and ampicillin against E. coli. According to the findings of the agar disk diffusion method, ampicillin had an inhibition zone radius of approximately 7 mm both in the dark and under the light. The inhibition zone under light irradiation was measured as 4.80 mm and 6 mm while 2.75 mm and 3 mm were measured for dark conditions for chlorophyll nanoparticles and chlorophyll gold nanoparticle conjugation respectively. This outcome confirms our earlier observations that these nanoparticles show minimal dark cytotoxicity nevertheless, the killing efficiency they showed toward bacteria is not as expected and remained at the 6 mm inhibition zone.

Scanning electron microscopy was used to better explore the interactions between nanoparticles and microorganisms (SEM). SEM is a trustworthy method for analyzing the morphology of bacteria in contact with any antibiotic substance. SEM pictures of E. coli that had been exposed to 8.60 µM for Chl and 7.49 µM FOR Chl-Au of nanoparticles both in the dark and under light were taken. E. coli cells treated with Chl and Chl-Au in the dark are shown below in Figure 3.26. It

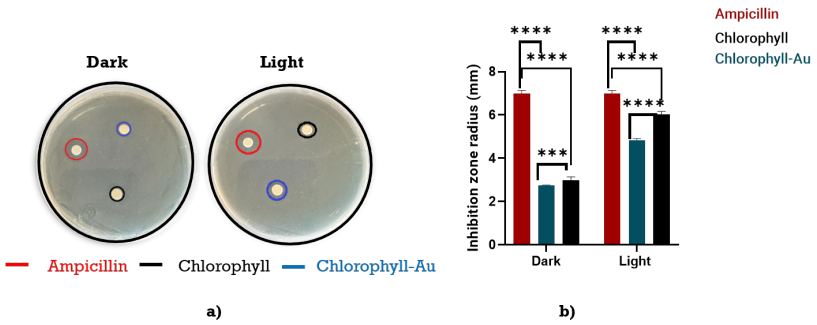

Figure 3.25: a) Plate photographs of agar disk diffusion assay of Chl and Chl-Au nanoparticles towards E. coli (indicated with blue) and ampicillin (indicated with red and black) in the dark and under light exposure. b) The corresponding inhibition zone radius graph of E. coli. Multiple paired t-test was conducted to compare results for the considerable differences between groups. (*** and **** demonstrate a remarkable difference between groups with $p < 0.001$ and $p < 0.0001$, respectively).

is evident from the photographs that the majority of the E. coli were rod-shaped. Unlike the case exposed to light, their cell walls kept their flat surfaces. The surface of the bacteria treated with NP collapsed. Similarly, with the illumination of white light, the shapes of S. aureus were disrupted and the deterioration of the cell wall is obviously seen in the image for Chl-Au. (Figure **??**)

3.2.5 Examination of Cytotoxicity and Photocytotoxicity on the MCF-7 Cell Line of Chl and Chl-Au Nanoparticles

The same results both with the literature and Chl nanoparticle were recorded. Chl-based nanoparticles significantly affect the MCF-7 cell line's cytotoxicity. While the cell viability of Chl nanoparticles at lower concentrations was high for the dark group, the cell viability declined with increasing concentration. This is hardly a substantial reduction, though. On the other hand, the MCF-7 cells displayed a striking reduction in cell viability when exposed to light. Figure 3.28 shows that even with 2.488 µM of Chl nanoparticle, there was a notable reduction when comparing samples treated with nanoparticles to the control group. Similar

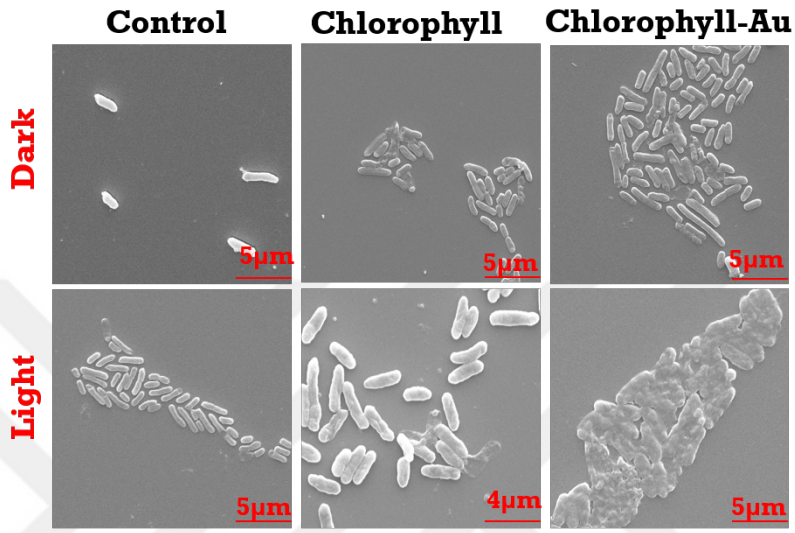

Figure 3.26: SEM images of E. coli treated with Chl and Chl-Au and non-treated in the dark and under white light exposure ($20mW/cm^2$) for 20 min.

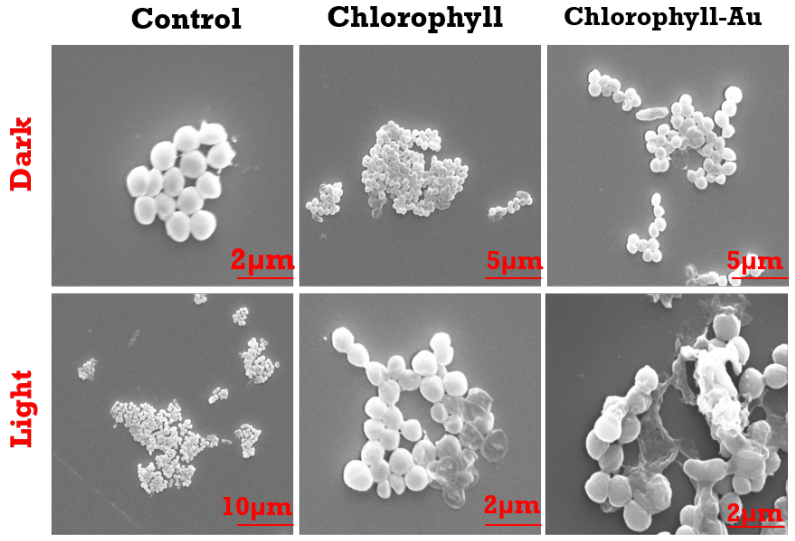

Figure 3.27: SEM images of S. aureus treated with Chl and Chl-Au and non-treated in the dark and under white light illumination ($20mW/cm^2$) for 20 min.

outcomes with a larger reduction in cell viability were seen for the MCF-7 cells treated with Chl-Au. Shaimaa Alexeree et all. reported that Chl b - Au NPs display a higher lethal effect on MCF-7 cell lines with an 80 % reduction under light irradiation and a 30 % reduction in the dark [52]. These results are much more promoting than our extracted chlorophyll nanoparticles. There might be two explanations for this; one of them is the composition of nanoparticles which resulted in the different connection between cellular walls; extracted chlorophyll contains both chlorophyll a and chlorophyll b; and also the preparation method of nanoparticles influences the results.

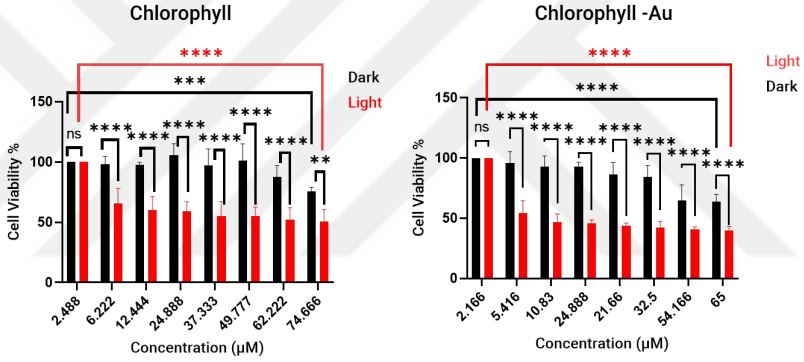

Figure 3.28: Relative cell viability (%) of Chl and Chl-Au against MCF-7 breast cancer cells at different concentrations in the dark and under light irradiation ($20mW/cm^2$, 20 minutes). 2-way ANOVA multiple comparison tests were performed to compare results for the considerable differences between groups. (** and **** express a remarkable difference between groups with $p < 0.0024$ and $p < 0.0001$, respectively).

3.2.6 Cellular Imaging by Chl and Chl-Au

The MCF-7 cell line was utilized to demonstrate the photodynamic anti-cancer impact of nanoparticles using the MTT assay. Confocal laser scanning microscopy (CLSM) was used to validate the MTT assay results and the interaction between cells and NPs. The NPs' inherent fluorescence qualities make them advantageous for application in image-guided PDT for cancer treatment or direct cellular imaging. To ascertain whether or not nanoparticles may be absorbed by MCF-7 cells, confocal laser scanning microscopy (CLSM) was employed to compare NP-treated

and untreated cells, as shown in Figure. The same applied to COL nanoparticles procedure was followed. DAPI emits blue fluorescence when excited by a 461 nm laser, whereas Chl and Chl-Au emit red fluorescence when excited by a 404 and 407 nm laser, respectively. The cellular absorption of nanoparticles was largely focused around the nuclear membrane, as seen in Figure 3.29.

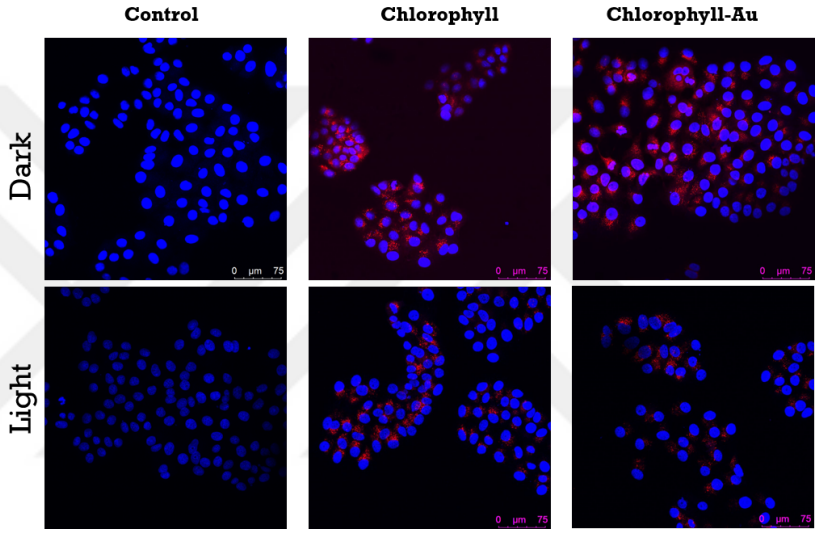

Figure 3.29: CLSM images of non-treated MCF-7 cells, Chl-treated cells and Chl-Au-treated cells.

Chapter 4

Conclusions and Future Works

Hereby, two different nanoparticles and their hybrid conjugation with gold nanoparticles were prepared successfully and their applications in a variety of nanomedicine fields comprising antimicrobial and anticancer PDT and cellular imaging were also demonstrated. Moreover, despite the fact that the gold nanoparticle was used to investigate photothermal therapy applications, the results were not satisfying therefore the photothermal effect of gold nanoparticle was ignored. Also, since gold nanoparticles displayed metal-enhanced ROS generation ability and provide higher efficiency, their effect was reported in this study. Firstly, in water, the stability of COL and COL-Au nanoparticles was recorded for a month without any seeable aggregation. Although they expressed high reactive oxygen species (ROS) production capacity the results for antibacterial applications were not as expected. The killing efficiency of nanoparticles was compared to ampicillin which has a 7 mm inhibition zone and the radius of the inhibition zone was measured as 4 mm and 5 mm for COL and COL-Au, respectively. Also, SEM was used to demonstrate the interaction between nanoparticles and bacterial cells. The aggregation of nanoparticles was observed in SEM images. Although better interaction and higher killing efficiency were obtained with the conjugation of gold nanoparticles, these nanoparticles did not exhibit higher efficiency compared to antibiotics. Future studies will be focused on modifying the conjugated

oligomer with re-synthesizing to solve both precipitation problems in the bacterial suspension and increase the killing effect against both Gram-positive and Gram-negative bacteria for both of the nanoparticles. Also, structure engineering of them will be required to enhance responsiveness with stimulation for active targeting and increasing photodynamic effect against antibacterial applications. On the other hand, COL demonstrated high killing efficiency under 20 min light illumination, and the reduction in the cell viability was recorded as 58 %, and displayed 18 % dark cytotoxicity. The higher reduction rates, 72 %, in the cell viability was recorded for COL-Au nanoparticles, with 40 % dark cytotoxicity. Although COL-Au has higher killing efficiency with light illumination, it is not a good photosensitizer because a good photosensitizer should have high killing efficiency with a little dark cytotoxicity. Secondly, in water, the stability of COL and COL-Au nanoparticles was recorded for a month without any seeable aggregation. Despite the poor solubility of chlorophyll in aqueous solutions, as indicated in the literature [69], water-dispersible nanoparticles were prepared by the nanoprecipitation method, and stability in an aqueous solution was obtained. After proving their high ROS generation ability, their antibacterial applications were studied against E. coli and S. aureus. By applying the surface plating method, a reduction up to 2.8-log and 2.33-log in colony-forming units (CFUs) was reported under light exposure for Chl-Au and Chl nanoparticles, respectively. On the other hand, 0.32-log and 0.15-log reductions in colony-forming units (CFUs) were measured under dark conditions. Furthermore, the inhibition zone of Chl and Chl-Au was measured as 4 mm and 5 mm. Also, the collapsing of the bacterial surface with light illumination was revealed by SEM images. However, it was expected to reach 7 mm like ampicillin. The reason for this might be poor solubility of chlorophyll in an aqueous medium might also affect and decrease killing efficiency. For anticancer photodynamic therapy applications, MCF-7 breast cancer cells were treated with these nanoparticles in the dark and under white light illumination for 20 minutes, and the reduction in cell viability was recorded with 50 % and 60 % reduction for light illumination, and 24 % and 36 % reduction in the dark for Chl and Chl-Au nanoparticles, respectively. Furthermore, the results display that the Au nanoparticles could increase the uptake, solubility, and PDT effect of nanoparticles. Also, the uptake of nanoparticles strongly and high efficiency were

verified by confocal microscopy. Since both of the nanoparticles showed higher levels of light-induced biocidal activity and relatively low dark cytotoxicity, they can be examined on other cancer cell lines. Furthermore, due to their naturally fluorescent qualities, they were also used in cellular imaging, and this property holds tremendous promise for image-guided PDT and drug delivery applications.

Bibliography

[1] R. E. Martin and F. Diederich, "Linear monodisperse π-conjugated oligomers: Model compounds for polymers and more," *Angewandte Chemie International Edition*, vol. 38, no. 10, pp. 1350–1377, 1999.

[2] C. Zhu, L. Liu, Q. Yang, F. Lv, and S. Wang, "Water-soluble conjugated polymers for imaging, diagnosis, and therapy," *Chemical Reviews*, vol. 112, no. 8, pp. 4687–4735, 2012. PMID: 22670807.

[3] S. Kim, C.-K. Lim, J. Na, Y.-D. Lee, K. Kim, K. Choi, J. F. Leary, and I. C. Kwon, "Conjugated polymer nanoparticles for biomedical in vivo imaging," *Chem. Commun.*, vol. 46, pp. 1617–1619, 2010.

[4] S. Thomas, G. Joly, and T. Swager, "Chemical sensors based on amplifying fluorescent conjugated polymers," *Chemical reviews*, vol. 107, pp. 1339–86, 05 2007.

[5] X. Feng, L. Liu, S. Wang, and D. Zhu, "Water-soluble fluorescent conjugated polymers and their interactions with biomacromolecules for sensitive biosensors," *Chem. Soc. Rev.*, vol. 39, pp. 2411–2419, 2010.

[6] S. Rasmussen, "On the origin of "synthetic metals": Herbert mccoy, alfred ubbelohde, and the development of metals from nonmetallic elements," *Bulletin for the history of chemistry / Division of the History of Chemistry of the American Chemical Society*, vol. 41, pp. 64–73, 12 2016.

[7] F. Zhang, D. Wu, Y. Xu, and X. Feng, "Thiophene-based conjugated oligomers for organic solar cells," *J. Mater. Chem.*, vol. 21, pp. 17590–17600, 2011.

[8] R. Abbel, R. van der Weegen, E. W. Meijer, and A. P. H. J. Schenning, "Multicolour self-assembled particles of fluorene-based bolaamphiphiles," *Chem. Commun.*, pp. 1697–1699, 2009.

[9] I. Fischer, A. Kaeser, M. A. M. Peters-Gumbs, and A. P. Schenning, "Fluorescent π-conjugated polymer dots versus self-assembled small-molecule nanoparticles: what's the difference?," *Chemistry*, vol. 19 33, pp. 10928–34, 2013.

[10] D. Tuncel, "π-conjugated nanostructured materials: preparation, properties and photonic applications," *Nanoscale Adv.*, vol. 1, pp. 19–33, 2019.

[11] X. Xu, R. Liu, and L. Li, "Nanoparticles made of π-conjugated compounds targeted for chemical and biological applications," *Chem. Commun.*, vol. 51, pp. 16733–16749, 2015.

[12] A. Imamura and Y. Aoki, "Molecular design of a π-conjugated single-chain electronically conductive polymer," *International Journal of Quantum Chemistry*, vol. 106, no. 8, pp. 1924–1933, 2006.

[13] "Fluorescence excitation and emission fundamentals."

[14] S. Griffin, M. I. Masood, M. J. Nasim, M. Sarfraz, A. P. Ebokaiwe, K.-H. Schäfer, C. M. Keck, and C. Jacob, "Natural nanoparticles: A particular matter inspired by nature," *Antioxidants*, vol. 7, no. 1, 2018.

[15] A. R. Battersby, "Tetrapyrroles: the pigments of life," *Nat. Prod. Rep.*, vol. 17, pp. 507–526, 2000.

[16] G. P. Moss, "Nomenclature of tetrapyrroles (recommendations 1986)," *Pure and Applied Chemistry*, vol. 59, no. 6, pp. 779–832, 1987.

[17] P. Ponka, "Cell biology of heme," *Research Journal of Medical Sciences*, vol. 318, pp. 241–256, 10 1999.

[18] T. Ott, J. T. van Dongen, C. Gu¨nther, L. Krusell, G. Desbrosses, H. Vigeolas, V. Bock, T. Czechowski, P. Geigenberger, and M. K. Udvardi, "Symbiotic leghemoglobins are crucial for nitrogen fixation in legume root nodules

but not for general plant growth and development," *Current Biology*, vol. 15, no. 6, pp. 531–535, 2005.

[19] N. Surmeli, "Optimization of hnox protein production in escherichia coli," *Cumhuriyet Science Journal*, vol. 38, pp. 86–97, 12 2017.

[20] M. O. Senge, A. Wiehe, and C. Ryppa, *Synthesis, Reactivity and Structure of Chlorophylls*, pp. 27–37. Dordrecht: Springer Netherlands, 2006.

[21] Q. Cai, Y. Fei, H.-W. An, X.-X. Zhao, Y. Ma, Y. Cong, L. Hu, L.-L. Li, and H. Wang, "Macrophage-instructed intracellular staphylococcus aureus killing by targeting photodynamic dimers," *ACS applied materials & interfaces*, vol. 10, p. 9197—9202, March 2018.

[22] A. Fercher, S. M. Borisov, A. V. Zhdanov, I. Klimant, and D. B. Papkovsky, "Intracellular o2 sensing probe based on cell-penetrating phosphorescent nanoparticles," *ACS Nano*, vol. 5, no. 7, pp. 5499–5508, 2011. PMID: 21671589.

[23] C. Pucci, C. Martinelli, A. Degl'Innocenti, A. Desii, D. De Pasquale, and G. Ciofani, "Light-activated biomedical applications of chlorophyll derivatives," *Macromolecular Bioscience*, vol. 21, no. 9, p. 2170027, 2021.

[24] P. Wang and B. Grimm, "Organization of chlorophyll biosynthesis and insertion of chlorophyll into the chlorophyll-binding proteins in chloroplasts," *Photosynthesis Research*, vol. 126, pp. 189 – 202, 2015.

[25] K.-Y. Pu and B. Liu, "Fluorescent conjugated polyelectrolytes for bioimaging," *Advanced Functional Materials*, vol. 21, no. 18, pp. 3408–3423, 2011.

[26] L. Feng, C. Zhu, H. Yuan, L. Liu, F. Lv, and S. Wang, "Conjugated polymer nanoparticles: preparation, properties, functionalization and biological applications," *Chem. Soc. Rev.*, vol. 42, pp. 6620–6633, 2013.

[27] H.-S. Peng and D. T. Chiu, "Soft fluorescent nanomaterials for biological and biomedical imaging," *Chem. Soc. Rev.*, vol. 44, pp. 4699–4722, 2015.

[28] G. Yang, F. Lv, B. Wang, L. Liu, Q. Yang, and S. Wang, "Multifunctional non-viral delivery systems based on conjugated polymers," *Macromolecular Bioscience*, vol. 12, no. 12, pp. 1600–1614, 2012.

[29] F. Wang, M. Li, B. Wang, J. Zhang, Y. Cheng, L. Liu, and F. Lv, "Synthesis and characterization of water-soluble polythiophene derivatives for cell imaging," *Scientific reports*, vol. 5, p. 7617, 01 2015.

[30] M. J. Webber and R. Langer, "Drug delivery by supramolecular design," *Chem. Soc. Rev.*, vol. 46, pp. 6600–6620, 2017.

[31] M. W. Tibbitt, J. E. Dahlman, and R. Langer, "Emerging frontiers in drug delivery," *Journal of the American Chemical Society*, vol. 138, no. 3, pp. 704–717, 2016. PMID: 26741786.

[32] R. Haag, "Supramolecular drug-delivery systems based on polymeric core–shell architectures," *Angewandte Chemie International Edition*, vol. 43, no. 3, pp. 278–282, 2004.

[33] F. Raymo and J. Stoddart, "Interlocked macromolecules," *American Chemical Society*, vol. 99, pp. 1634–1664, 07 P1999.

[34] S. Nepogodiev and J. STODDART, "Cyclodextrin-based catenanes and rotaxanes," *Chemical reviews*, vol. 98, pp. 1959–1976, 06 1998.

[35] P. T. Glink, A. I. Oliva, J. F. Stoddart, A. J. P. White, and D. J. Williams, "Template-directed synthesis of a [2]rotaxane by the clipping under thermodynamic control of a crown ether like macrocycle around a dialkylammonium ion," *Angewandte Chemie International Edition*, vol. 40, no. 10, pp. 1870–1875, 2001.

[36] P. Rajakumar and R. Anandhan, "Synthesis and in-vitro anti-inflammatory activity of novel glycodendrimers with benzene 1,3,5 carboxamide core and triazole as branching unit," *European journal of medicinal chemistry*, vol. 46, p. 4687—4695, September 2011.

[37] S. Cecioni, V. Oerthel, J. Iehl, M. Holler, D. Goyard, J.-P. Praly, A. Imberty, J.-F. Nierengarten, and S. Vidal, "Synthesis of dodecavalent fullerene-based

glycoclusters and evaluation of their binding properties towards a bacterial lectin," *Chemistry – A European Journal*, vol. 17, no. 11, pp. 3252–3261, 2011.

[38] K. R. Bortoluci and R. Medzhitov, "Control of infection by pyroptosis and autophagy: role of tlr and nlr," *Cellular and Molecular Life Sciences*, vol. 67, pp. 1643–1651, 2010.

[39] N. Sharon, "Lectin-carbohydrate complexes of plants and animals: an atomic view," *Trends in Biochemical Sciences*, vol. 18, no. 6, pp. 221–226, 1993.

[40] E. S. Shibu, M. Hamada, N. Murase, and V. Biju, "Nanomaterials formulations for photothermal and photodynamic therapy of cancer," *Journal of Photochemistry and Photobiology C: Photochemistry Reviews*, vol. 15, pp. 53–72, 2013. Next Generation Photochemistry from Asia.

[41] T. Ajiboye, "What is phototherapy?."

[42] X. Li, J. F. Lovell, J. Yoon, and X. Chen, "Clinical development and potential of photothermal and photodynamic therapies for cancer," *Nature reviews. Clinical oncology*, vol. 17, p. 657—674, November 2020.

[43] T. Maisch, "A new strategy to destroy antibiotic resistant microorganisms: antimicrobial photodynamic treatment.," *Mini reviews in medicinal chemistry*, vol. 9 8, pp. 974–83, 2009.

[44] B. C. Wilson and M. S. Patterson, "The physics, biophysics and technology of photodynamic therapy," *Physics in Medicine & Biology*, vol. 53, p. R61, apr 2008.

[45] Y.-J. Hou, X.-X. Yang, R.-Q. Liu, D. Zhao, C.-X. Guo, A.-C. Zhu, M.-N. Wen, Z. Liu, G.-F. Qu, and H.-X. Meng, "Pathological mechanism of photodynamic therapy and photothermal therapy based on nanoparticles," *International journal of nanomedicine*, vol. 15, pp. 6827–6838, 09 2020.

[46] N. Samuel, L. Ombaka, E. Masika, and M. Ng'ang'a, "Antimicrobial photodynamic activity of phthalocyanine derivatives," *Advances in Chemistry*, vol. 2018, pp. 1–8, 03 2018.

[47] M. Özkan, "Cucurbituril-based supramolecular constructs for the diverse applications of nanomedicine," Master's thesis, Bilkent University, 08 2020.

[48] M. Özkan, S. E. Hadi, I. Tunç, Y. Midilli, B. Ortaç, and D. Tuncel, "Cucurbit[7]uril-capped hybrid conjugated oligomer-gold nanoparticles for combined photodynamic-photothermal therapy and cellular imaging," *ACS Applied Polymer Materials*, vol. 2, no. 9, pp. 3840–3849, 2020.

[49] Y. Zhao, Z. Zhang, Z. Lu, H. Wang, and Y. Tang, "Enhanced energy transfer in a donor–acceptor photosensitizer triggers efficient photodynamic therapy," *ACS Applied Materials & Interfaces*, vol. 11, no. 42, pp. 38467–38474, 2019. PMID: 31553165.

[50] B. H. Song, D. H. Lee, B. C. Kim, S. H. Ku, E. joo Park, I. H. Kwon, K. ho Kim, and K. joong Kim, "Photodynamic therapy using chlorophyll-a in the treatment of acne vulgaris: a randomized, single-blind, split-face study.," *Journal of the American Academy of Dermatology*, vol. 71 4, pp. 764–71, 2014.

[51] A. Castano, P. Mroz, and M. Hamblin, "Photodynamic therapy and tumor immunity," *Nature reviews. Cancer*, vol. 6, pp. 535–45, 08 2006.

[52] S. Alexeree, H. E. ElZorkany, Z. Abdel-Salam, and M. A. Harith, "A novel synthesis of a chlorophyll b-gold nanoconjugate used for enhancing photodynamic therapy: In vitro study," *Photodiagnosis and Photodynamic Therapy*, vol. 35, p. 102444, 2021.

[53] Y.-C. Chin, L.-X. Yang, F.-T. Hsu, C.-W. Hsu, T.-W. Chang, H.-Y. Chen, L. Chen, Z. Chia, C.-H. Hung, W.-C. Su, Y.-C. Chiu, C.-C. Huang, and M.-Y. Liao, "Iron oxide@chlorophyll clustered nanoparticles eliminate bladder cancer by photodynamic immunotherapy-initiated ferroptosis and immunostimulation," *Journal of Nanobiotechnology*, vol. 20, 08 2022.

[54] R. Liu, L. Zhang, J. Zhao, C. Hou, Y. Huang, Z. Huang, and S. Zhao, "A distinctive spinach-based carbon nanomaterial with chlorophyll-rich and

near-infrared emission for simultaneous in vivo biothiol imaging and dual-enhanced photodynamic therapy of tumor," *Advanced Therapeutics*, vol. 2, no. 7, p. 1900011, 2019.

[55] WHO, "Antimicrobial resistance."

[56] A. Petchiappan and D. Chatterji, "Antibiotic resistance: Current perspectives," *ACS Omega*, vol. 2, pp. 7400–7409, 10 2017.

[57] P. Vikesland, E. Garner, S. Gupta, S. Kang, A. Maile-Moskowitz, and N. Zhu, "Differential drivers of antimicrobial resistance across the world," *Accounts of Chemical Research*, vol. 52, pp. 916–924, 03 2019.

[58] G. D. Wright, "Molecular mechanisms of antibiotic resistance," *Chem. Commun.*, vol. 47, pp. 4055–4061, 2011.

[59] X. Li, B. Wu, H. Chen, K. Nan, Y. Jin, L. Sun, and B. Wang, "Recent developments in smart antibacterial surfaces to inhibit biofilm formation and bacterial infections," *J. Mater. Chem. B*, vol. 6, pp. 4274–4292, 2018.

[60] X. Li, H. Bai, Y. Yang, J. Yoon, S. Wang, and X. Zhang, "Supramolecular antibacterial materials for combatting antibiotic resistance," *Advanced Materials*, vol. 31, no. 5, p. 1805092, 2019.

[61] R. Peng, Y. Luo, Q. Cui, J. Wang, and L. Li, "Near-infrared conjugated oligomer for effective killing of bacterial through combination of photodynamic and photothermal treatment," *ACS Applied Bio Materials*, vol. 3, no. 2, pp. 1305–1311, 2020. PMID: 35019331.

[62] V. Soltaninejad, M. R. Ahghari, R. Taheri-Ledari, and A. Maleki, "Bifunctional pva/zno/agi/chlorophyll nanocomposite film: Enhanced photocatalytic activity for degradation of pollutants and antimicrobial property under visible-light irradiation," *Langmuir*, vol. 37, no. 15, pp. 4700–4713, 2021. PMID: 33821643.

[63] E. D. Soner, "Design and synthesis of monosaccharide functionalized conjugated polymers, polyrotaxanes and oligomers for biological applications," Master's thesis, Bilkent University, 09 2015.

[64] T. Riss, A. Niles, and L. Minor, "Cell viability assays assay guidance manual," *Assay Guid. Man.*, pp. 1–23, 01 2004.

[65] T. Balkan, S. Kizir, and D. Tuncel, "One-pot synthesis of hybrid conjugated oligomer-ag nanoparticles," *ACS Omega*, vol. 2, pp. 5470–5477, 09 2017.

[66] C.-Y. Hsu, P.-Y. Chao, S.-P. Hu, and C.-M. Yang, "The antioxidant and free radical scavenging activities of chlorophylls and pheophytins," *Food and Nutrition Sciences*, vol. 04, pp. 1–8, 01 2013.

[67] D. Sengupta, B. Mondal, and K. Mukherjee, "Visible light absorption and photo-sensitizing properties of spinach leaves and beetroot extracted natural dyes," *Spectrochimica Acta Part A: Molecular and Biomolecular Spectroscopy*, vol. 148, pp. 85–92, 2015.

[68] V. Rizzi, D. Vurro, T. Placido, P. Fini, A. Petrella, P. Semeraro, and P. Cosma, "Gold-chlorophyll a-hybrid nanoparticles and chlorophyll a/cetyltrimethylammonium chloride self-assembled-suprastructures as novel carriers for chlorophyll a delivery in water medium: Photoactivity and photostability," *Colloids and Surfaces B: Biointerfaces*, vol. 161, pp. 555–562, 2018.

[69] M. Martins, C. M. Albuquerque, C. F. Pereira, J. A. P. Coutinho, M. G. P. M. S. Neves, D. C. G. A. Pinto, M. A. F. Faustino, and S. P. M. Ventura, "Recovery of chlorophyll a derivative from spirulina maxima: Its purification and photosensitizing potential," *ACS Sustainable Chemistry & Engineering*, vol. 9, no. 4, pp. 1772–1780, 2021.